Journal of Sedimentary Research

SEPM
1926
Society for
Sedimentary Geology

RED-BED BLEACHING IN A CO$_2$ STORAGE ANALOGUE: INSIGHTS FROM ENTRADA SANDSTONE FRACTURE-HOSTED MINERALIZATION

JEREMY C. RUSHTON,[1] DORIS WAGNER,[1] JONATHAN M. PEARCE,[1] CHRISTOPHER A. ROCHELLE,[1] AND GEMMA PURSER[2]

[1]*British Geological Survey, Kingsley Dunham Centre, Keyworth, Nottingham NG12 5GG, U.K.*
[2]*The University of Edinburgh, School of Earth Sciences, The King's Buildings, James Hutton Road, Edinburgh EH9 3FE, U.K.*
e-mail: jere1@bgs.ac.uk

ABSTRACT: Improving our ability to predict the interactions between CO$_2$ and reservoir rocks at geological time scales is of key importance if carbon capture and storage (CCS) is to have a role in climate-change mitigation, particularly in the light of likely regulatory requirements. Understanding and identifying the relevant geological processes over long time scales can be obtained only at natural-analogue sites. At one such site, in the Salt Wash Graben area of Utah, USA, widespread bleaching affects the Middle Jurassic red-bed "wet dune" Entrada Sandstone. Previous work has proposed a genetic link between the bleaching and spatially concomitant recent and modern CO$_2$-rich fluids. The results presented here challenge some of the previous models and come from a detailed petrographic examination of mineralized fractures in the Entrada Sandstone that are centered in vertical extensions to the bleaching. These fractures typically contain complex mineralization assemblages. Pyrite was a paragenetically early phase, identifiable from common pseudomorphs of mixed iron oxides and oxyhydroxides that rarely contain relict pyrite. The pyrite contains up to 3 wt% arsenic. The volume of fracture-adjacent bleached sandstone is sufficient to have been the source of iron for the pyrite originally present in the fracture. The pyrite pseudomorphs occur at the center of fracture- and pore-filling cements that comprise intergrowths of hematite–goethite–jarosite–gypsum, an assemblage that suggests that their formation resulted from the oxidative alteration of pyrite, a genetic link supported by the arsenic present in the iron-bearing minerals. The presence of jarosite and proximal removal of earlier, sandstone-hosted carbonates are consistent with, and indicative of, the low-pH conditions associated with pyrite oxidation reactions. Calcite- and gypsum-cemented fractures crosscut, and contain fragments of, the pyrite-pseudomorphic and -oxidation assemblages, proving that they postdate pyrite formation and its subsequent oxidation, and that pyrite oxidation was not a result of modern weathering reactions. In outcrop, some calcite- and gypsum-cemented fractures link with travertine deposits associated with the modern and recent CO$_2$-rich fluids. The mineral assemblages observed here, and the paragenetic sequence that we have inferred, suggest that the fracture-associated bleaching patterns result from the fracture-fed movement of sulfur-bearing reducing fluids, with hydrogen sulfide the most likely bleaching agent. We conclude that bleaching adjacent to fractures is not genetically related to modern CO$_2$-bearing fluids despite the spatial relationship. The bleaching was already present when the modern fluids utilized the same fracture-based fluid pathways. We suggest that the more widespread regional bleaching formed contemporaneously with the fracture bleaching and followed similar mechanisms. This study highlights the complexity of interpreting analogue sites and the importance of using field and petrographic observations to unravel textures and events that are juxtaposed spatially but not temporally.

INTRODUCTION

The primary objective of the research presented here is to improve the understanding of the interaction between geological materials and carbon dioxide (CO$_2$) at a geological time scale. This, in turn, is intended to reduce the uncertainties inherent in predicting the outcomes of the long-term storage (tens of thousands of years and beyond) of CO$_2$ in the subsurface as part of a carbon capture and storage (CCS) approach to the mitigation of greenhouse-gas emission to the atmosphere.

The agreement that was reached at the December 2015 Paris UN Climate Change Conference (COP21–CMP11), to work towards the recommendation that global warming should be limited to 2°C by 2100,

highlights the relevance of these research aims. The recommendation, from the Inter-Government Panel on Climate Change (IPCC), is designed to avoid serious and damaging climate side effects (IPCC 2014). To this end, net emissions of greenhouse gases to the atmosphere need to be reduced by between 40 and 70% (relative to 2010) by 2050. Reducing the level of atmospheric CO$_2$, for which CCS could be a key contributor, is recognized as a major requirement to achieve this target (Pacala and Socolow 2004; IPCC 2005).

In order to proceed with a CCS installation, it must meet regulatory requirements. For example, EU DIRECTIVE 2009/31/EC states "that the stored CO$_2$ will be completely and permanently contained." Whilst the shorter-time-scale aspects of such storage requirements can be assessed
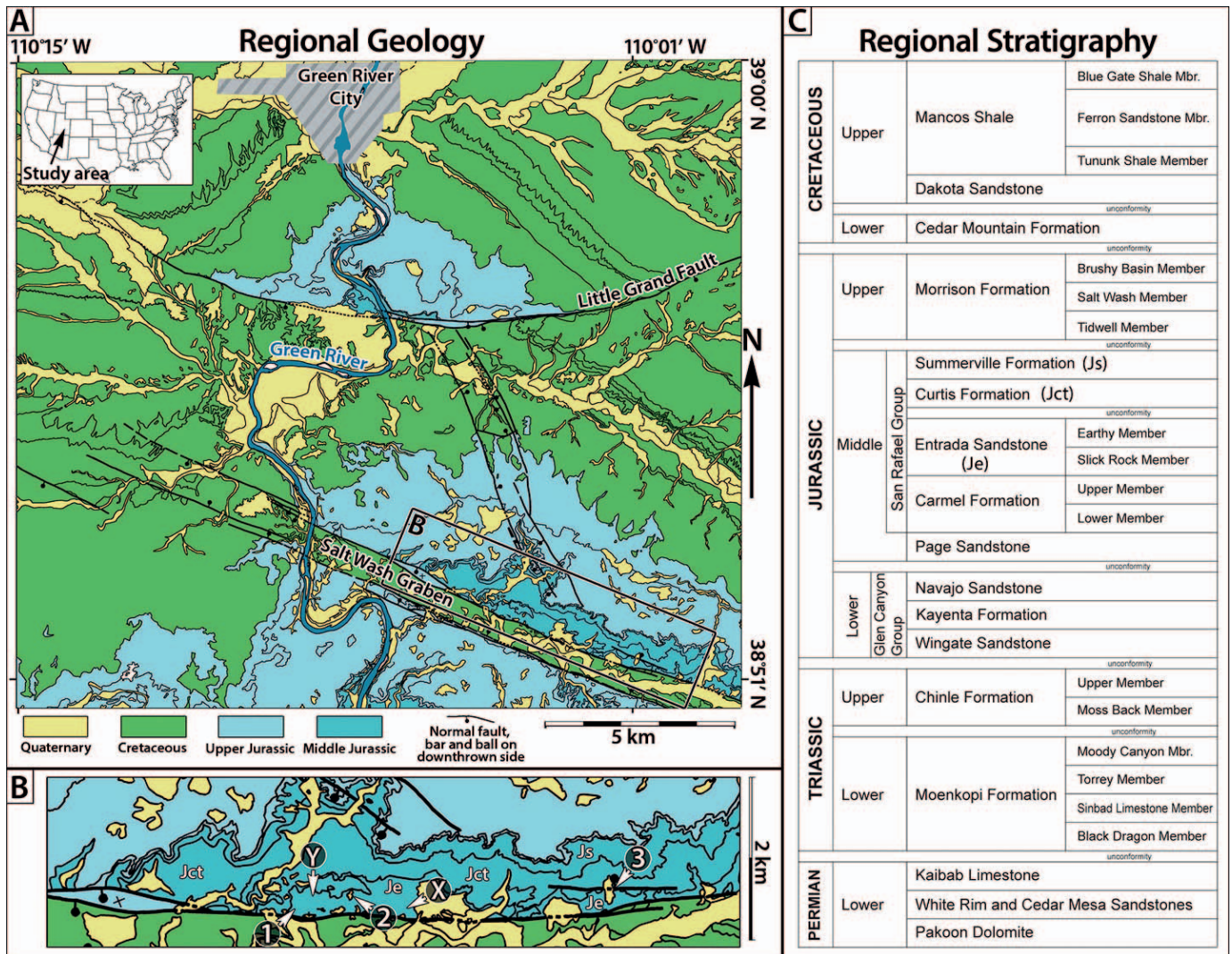
Fig. 1.—Geological map and stratigraphy of the study area. **A)** A simplified geological map of the study area, adapted from Doelling (2002). The boxed area shows the location of Part B. **B)** Detail of the study area with locations of sample sites, same key as for Part A. Numbers 1, 2, and 3 are the three fracture sites and X and Y are locations of the XRF and XRD profiles, respectively, as described in Table 1. All sites are hosted in Entrada Sandstone. Middle Jurassic subdivisions are marked Je, Jct, and Js for the Entrada Sandstone, Curtis and Summerville formations, respectively. **C)** Regional stratigraphy adapted from Doelling (2002).

relatively readily with experimental studies, the longer, geological, time scales implicit in the term "permanent" cannot be assessed experimentally, without incurring high degrees of uncertainty. Some natural accumulations of CO_2 can, however, be considered analogous to subsurface CO_2 repositories, and can therefore be used as "natural analogues" for the geological-storage concept (Pearce et al. 1996; Baines and Worden 2004; Zhou et al. 2012). Analyses of these systems will in turn contribute to reducing the uncertainties in security of storage necessary for potential operators of CCS facilities to be confident of meeting regulatory requirements. These considerations are covered well by other authors (Pearce et al. 1996; Parry et al. 2007; Zhou et al. 2012; Kampman et al. 2014).

The research presented here was part of such a CCS analogue study, in this case looking at outcrop samples of Middle Jurassic sandstones in the Green River area of Utah, USA (Fig. 1A). The Colorado Plateau, within which the Green River study area lies, contains numerous natural accumulations of CO_2 (Allis et al. 2001), together with CO_2-rich springs and geysers, and recent and modern carbonate travertine deposits (Allis et al. 2002). It has therefore become a center of interest for CCS natural-

analogue research (Shipton et al. 2004; Haszeldine et al. 2005; Parry et al. 2007; Kampman et al. 2009, 2014; Wigley et al. 2012, 2013; Zhou et al. 2012).

The Jurassic rocks of the Green River area are well known for their strong red color, which is associated with the presence of hematite (Walker 1967; Walker et al. 1978), and localized bleaching where the hematite has been removed (Foxford et al. 1996; Allis et al. 2001; Chan et al. 2001; Garden et al. 2001). Fractures in the same rocks have bleaching patterns that show that they have acted as vertical conduits for bleaching fluids. Some workers have suggested that there is a link between recent CO_2-rich fluids and this red-bed bleaching (Allis et al. 2001; Wigley et al. 2013; Kampman et al. 2014; Ogata et al. 2014).

Of key interest at the study site is the fate of the iron; its reduction and mobilization is implied by the bleaching patterns. If CO_2 is involved in either of these processes then there are important implications for CCS, since many of the reservoir formations being considered for CCS installations are in red-bed sedimentary rocks. A CO_2-driven bleaching mechanism, which could result in the permanent fixing of some CO_2 in

TABLE 1.—*List of sample sites, sample identifiers, and analyses performed. Sample site locations are shown in Figure 1B and fracture-site locations in Figure 2.*

Sample Site	Field/Sample Code(S)	Site Description	Samples Taken	Analyses
Site X	JMPE37,39,40	A 15 m × 25 m site containing Entrada Sandstone with typical nearly horizontal regional bleaching, cut by subvertical bleached fractures.	MPLP132 to 135. A set of bleached and unbleached samples, including one of the bleaching contact.	XRF (Table 2)
Profile Y	JMPE63	Low bluff (3 m) with a horizontal contact between red (above) and bleached (below) Entrada Sandstone.	MPLP543 to 549. A sequence through the contact: three in the red, three in the bleached, and one at the contact.	XRD (Table 3), OM, SEM, CL
Fracture 1	MPLR916	13-m-high butte of Entrada Sandstone, bleached to about 8–9 m. Several fracture clusters run the full height of the butte and are at the centers of bleached zones.	The mineralized fracture and immediately adjacent wall rock.	XRD, OM, SEM
Fracture 2	JMPE72	Vertical fracture in ~ 4 m cliff outcrop of massive and horizontally bedded Entrada Sandstone, capped by a travertine deposit.	A sequence from and including the mineralized fracture through the bleached interval to the red sandstone.	XRD (Table 3), OM, SEM, CL
Fracture 3	JMPE95	One of many subvertical fractures in ~ 6 m cliff outcrop of horizontally bedded red silty Entrada Sandstone, capped by Curtis Formation.	One of the mineralized fractures, one from the associated contact between bleached and red sandstone.	XRD (Table 4), OM, SEM

consequent iron carbonate precipitates, would make red-bed reservoir formations very attractive to CCS operators.

In order to elucidate the potential involvement of CO_2 in the reduction of iron and/or its subsequent migration, we have used field observations and detailed petrography to determine a paragenetic sequence for the fractures and their associated bleaching and mineralization.

GEOLOGICAL CONTEXT

Rocks in the study area (Fig. 1A, B) form part of the fill of the Paradox Basin, which lies within the Colorado Plateau, USA. The geological history of the Colorado Plateau is well established (Stokes 1986; Hintze 1988) and the stratigraphy (Fig. 1C) consists of approximately 2400 m of Permian eolian and fluvial deposits at its base. The overlying Triassic sedimentary rocks include the coastal Moenkopi Formation and fluvial and lacustrine deposits of the Chinle Formation. The eolian and fluvial sheet-flood sandstones of the Wingate Sandstone and Kayenta Formation, respectively, span the Triassic–Jurassic boundary. Thick dune deposits of the Navajo Sandstone and the overlying Entrada Sandstone are locally separated by the heterogeneous sabkha sequence of the Carmel Formation (Parry et al. 2007) and are unconformably overlain by the Curtis and Summerville formations. The Carmel to Summerville Formation sequence is collectively known as the San Rafael Group (Fig. 1C). The Jurassic sequence is topped by the Morrison Formation, and this is overlain by the Cretaceous Cedar Mountain Formation (Doelling 2002).

The period of deposition during which the Jurassic and Cretaceous rocks accumulated was related to Mesozoic eastward-dipping subduction in a NNE–SSW foreland basin. Breit and Goldhaber (1996) show that from the mid-Cretaceous to the mid-Tertiary, the Upper Jurassic of the Paradox Basin was progressively buried to a maximum depth between 2.5 and 4 km, and the last 6 Ma has seen the Colorado Plateau subsequently uplifted by 2 km (Nuccio and Condon 1996).

The study area is confined to a segment of Middle Jurassic outcrop to the north of the graben-bounded Salt Wash creek (Fig. 1A). The Salt Wash Graben is a WNW–ESE-trending structure to the south of the city of Green River, which cuts across a north-dipping anticline. It lies to the south of the "Crystal Geyser," and on its northern margin has several CO_2-rich springs and abundant travertine deposits (Allis et al. 2002). The Graben boundary faults are sets of en echelon normal-fault systems, which offset the Jurassic sedimentary rocks in their footwalls to the north and south against Cretaceous sedimentary rocks at the center (Doelling 2002). Ogata et al.

(2014) have characterized the fracture systems in the area. It has been suggested that the Salt Wash faults form an extension to the Moab fault, which lies to the southeast (Shipton et al. 2004). Work by Kampman et al. (2012) suggests that the faults in the region have opened periodically in the last 135,000 years at glacial–interglacial transitions.

Rocks of the Slick Rock and Earthy members of the Entrada Sandstone crop out in the study area. The core of the anticline immediately to the north of the Salt Wash Graben (Doelling 2001, 2002; Newell and Butcher 2015) exposes 20–30 m of the Slick Rock Member overlying the Earthy member, the base of which is not exposed. Although Doelling (2001) has not differentiated these members in the study area, the recent work of Newell and Butcher (2015) has recognized, mapped, and characterized them in part of the study area. McKnight (1940) also recognized local facies in the Entrada Sandstone east of the Green River and specifically to the north of the of the Salt Wash graben block, describing a muddy, "earthy facies," sandstone at the top of the Entrada Sandstone in these areas. The Entrada Sandstone is locally extensively bleached, the bleaching being most pronounced towards the base of the stratigraphically lowest exposed strata. The bleaching extends upwards into stratigraphically younger rocks, such as the Curtis and Summerville formations, along the margins of the common faults in the area.

Entrada Sandstone Depositional Environments

The Entrada Sandstone to the east of Green River has been identified as a continental deposit, dominated by eolian conditions (McKnight 1940; Kocurek 1981; Doelling 2001; Garden et al. 2001) which can locally be further subdivided into the Slick Rock and Earthy members (Fig. 1C). The Slick Rock Member contains common well rounded grains, is quartz-dominated and clay-poor, and commonly displays high-angle cross-bedding with some wind ripples, all consistent with this interpretation (Doelling 2001; Newell and Butcher 2015). Intercalated with these "clean dune" deposits are sandstones and siltstones with wavy or convolute laminations that are locally clay-rich; these are interpreted to represent damp and wet interdune deposits with localized sabkha development (Kocurek 1981; Crabaugh and Kocurek 1993; Newell and Butcher 2015). The Earthy member is a finer-grained unit that sharply overlies the Slick Rock Member. It typically comprises a mix of sand, silt, and clay, with lenticular decimeter-scale sand bodies separated by laminated fine sands, silts and clays (Newell and Butcher 2015). Kocurek (1981) has interpreted these as arid marine-margin sabkha or mudflat deposits. The Entrada

Sandstone as a whole in the study area is considered a classic example of a "wet eolian dune system" (Crabaugh and Kocurek 1993).

A Note on Terminology

The following terms are used throughout:

- Host Rock: The rock that has been fractured; in the study area this is the Entrada Sandstone and rocks of the immediately overlying Curtis Formation. Host rock samples are those that do not contain any of the mineralized fracture material and which are not directly in contact with mineralized fractures.
- Fracture Rock: This is rock material that includes the fracture mineralization itself. It also includes the fragments of host rock that have become entrained within, and cemented by, the mineralization, as well as those that are present between fractures where there are several subparallel mineralized fractures.
- Wall Rock: Rock that is in direct contact with a mineralized fracture but which does not contain the fracture. For the purposes of the descriptions below, this fracture contact face and the immediately adjacent 2–3 cm are considered to be "wall rock."

Field Sampling

Rock samples were taken from three fracture sites (1, 2, and 3 in Fig. 1B, shown in Fig. 2) from outcrops in the northern margin of the Salt Wash Graben. All of the fracture sites are within the Entrada Sandstone (Fig. 1B). At each of the fracture locations the red host rocks are sandstones with bleaching patterns that are regionally subhorizontal (Fig. 2), but track intersecting fractures with sub-bedding-scale irregularities (Fig. 2). At sites 2 and 3, samples were collected from the unbleached and bleached elements of the host rock, as well as from the fracture-mineralization zone with included wall-rock material. At site 1 the part of the fracture that was sampled was from within a bleached horizon in the host rock (Fig. 2A, B), so only samples of fracture-mineralization and immediately adjacent wall rock were collected. Two of the samples (from sites 2 and 3) come from fractures that run parallel to the Salt Wash faults that bound the Salt Wash Graben.

Dark brown, ochre, and red mineralization is typically found at the fracture centers (Fig. 2D, F), with variable proportions of subparallel white veins (Fig. 2D). The white veins locally diverge from the main fracture. There are typically diffuse ochreous zones that affect the bleached material immediately adjacent to the fracture fills, showing decreasing intensity with increasing distance from the fill; this is particularly shown at site 2 (Fig. 2D). At one of the three sites (Site 2, Fig. 2C), the fracture links to a travertine deposit at the top of the exposure.

ANALYTICAL METHODS

The petrographic work presented here is based primarily on a range of scanning-electron and optical-microscopic techniques (SEM and OM respectively), the former supported by energy-dispersive X-ray analysis (EDXA), with mineralogy from X-ray diffraction (XRD) analysis, and bulk chemistry from X-ray fluorescence (XRF) analysis. See the methods Appendix for full details.

RESULTS: HOST ROCK CHEMISTRY, MINERALOGY, AND PETROGRAPHY

Bulk Chemistry: XRF Data

Data from these analyses is shown in Table 2. This data is from a site (X in Fig. 1B) that has many features in common with the fracture sites. There are mineralized fractures with bleached margins at outcrops capped by travertine deposits. This analytical profile records the bulk chemistries of

TABLE 2.—XRF-derived major-element content in weight % for red and bleached Entrada Sandstone samples from sample site X (Figure 1B). Fe_2O_3t represents total iron expressed as Fe_2O_3. SO_3 represents sulfur retained in the fused bead. LOI is loss on ignition. Data is accurate to three significant figures. There is a detection limit of 0.01% to most oxides (exception SO_3). Values < 1% are considered accurate to two decimal places.

| Sample Site: Number	Sample Color	SiO_2	TiO_2	Al_2O_3	Fe_2O_3t	Mn_3O_4	MgO	CaO	Na_2O	K_2O	P_2O_5	SO_3	Cr_2O_3	SrO	ZrO_2	BaO	NiO	CuO	ZnO	PbO	LOI	Total
X: MPLP132	Red	76.4	0.27	6.02	1.15	0.04	1.33	5.10	0.30	2.24	0.06	< 0.1	< 0.01	0.02	0.04	0.03	< 0.01	< 0.01	< 0.01	< 0.01	6.50	99.52
X: MPLP135	Red	77.0	0.34	6.41	1.25	0.03	1.37	4.46	0.32	2.35	0.08	< 0.1	< 0.01	0.02	0.06	0.03	< 0.01	< 0.01	< 0.01	< 0.01	6.16	99.89
X: MPLP135	Bleached	77.7	0.34	6.53	0.97	0.03	1.33	4.20	0.32	2.40	0.08	< 0.1	< 0.01	0.02	0.06	0.03	< 0.01	< 0.01	< 0.01	< 0.01	5.78	99.83
X: MPLP134	Bleached	78.5	0.27	6.12	0.90	0.04	1.36	4.41	0.23	2.29	0.07	< 0.1	< 0.01	0.02	0.04	0.03	< 0.01	< 0.01	< 0.01	< 0.01	5.84	100.09
X: MPLP133	Bleached	79.2	0.29	6.23	0.94	0.03	1.30	3.87	0.24	2.32	0.07	< 0.1	< 0.01	0.02	0.05	0.03	< 0.01	< 0.01	< 0.01	< 0.01	5.38	99.94
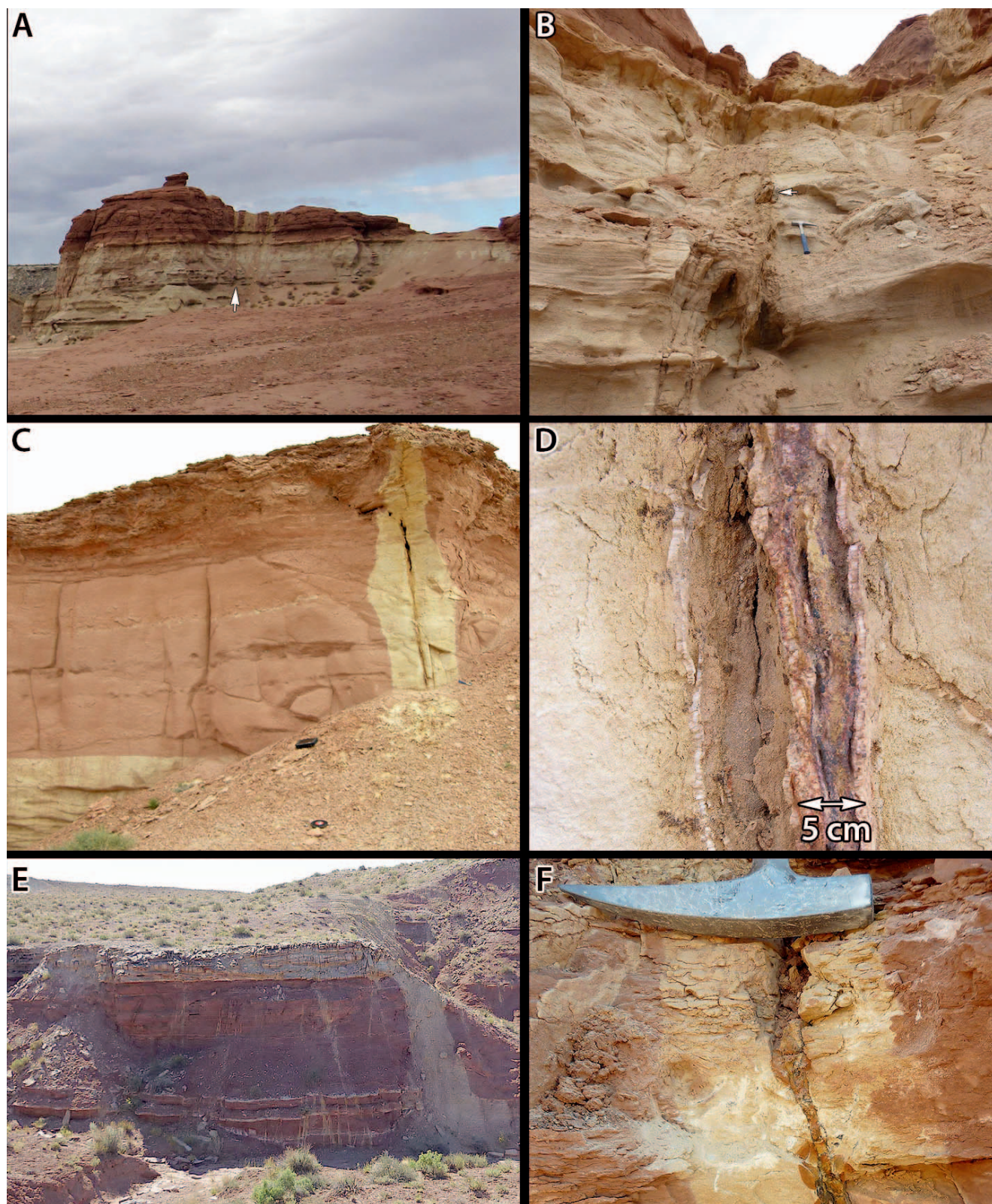
FIG. 2.—Field photos of sampled fracture sites and details of the fractures. **A)** At site 1, most of the ~ 13-m-high outcrop is bleached. The arrow marks the location of Part B. The bleaching associated with the fractures carries through the largely unbleached outcrop cap. **B)** Detail of the site 1 fracture sample location looking along the cluster of mineralized fractures. Hammer shaft is 33 cm long. Arrow is precise sample point. **C)** Location of site 2. The ~ 4 m cliff outcrop is of massive and horizontally bedded Entrada Sandstone and is capped by a travertine deposit. Note the nearly horizontal contact between bleached and unbleached sandstone, lower left. **D)** Detail of site 2 fracture, showing its composite form and the multicolored nature of the mineralization. Ochreous staining is strongest at the center and fades with increased distance into the host rock. **E)** Site 3 is the easternmost location, comprising a largely unbleached and thinly horizontally bedded sequence of silty sandstones. Bleaching at the top of the ~ 6-m-high outcrop is linked to subvertical fractures, the largest of which is at the right of the outcrop. Smaller more thinly bleached fractures are abundant across the face and cut across bed-bounded older bleached layers. **F)** Detail of the site 3 sampled fracture, one of the finer subvertical fractures in Part E. Hammer head is 20 cm long.

TABLE 3.—*XRD-derived bulk mineral analysis from Entrada Sandstone samples taken across a horizontal red–bleached contact and a vertical red–bleached contact from profile Y and site 2, respectively (Fig. 1B). Positive distances are in the red sandstone, and negative distances are in the bleached sandstone.*

Sample site: sample number	Sample color	Distance (cm) from bleaching contact	Silicates					Carbonates		Oxide	Chloride
			Quartz	K-feldspar	Albite	Kaolin[1]	Mica[2]	Calcite	Dolomite	Hematite	Halite
Y: MPLP549	Red	+60	83.1	4.9	0.6	< 0.5	4.5	2.2	4.0	< 0.5	< 0.5
Y: MPLP548	Red	+30	82.2	4.9	0.5	< 0.5	4.2	3.7	3.9	< 0.5	nd
Y: MPLP546	Red	+10	82.1	5.1	0.7	< 0.5	4.5	2.4	4.5	< 0.5	nd
Y: MPLP545	Red	0	80.6	5.1	0.8	< 0.5	5.3	3.2	4.3	< 0.5	nd
Y: MPLP545	Bleached	0	81.2	4.9	1.0	< 0.5	5.2	3.5	3.9	nd	nd
Y: MPLP543	Bleached	−10	82.0	5.1	0.8	< 0.5	5.3	2.5	4.0	nd	nd
Y: MPLP544	Bleached	−30	81.7	5.4	0.6	< 0.5	5.1	2.6	4.3	nd	nd
Y: MPLP547	Bleached	−60	81.2	5.3	0.8	< 0.5	5.1	2.4	4.8	nd	< 0.5
2: MPLP555	Red	+115	78.2	6.0	1.4	< 0.5	5.7	2.5	4.0	< 0.5	1.4
2: MPLP553	Red	0	79.8	6.1	1.0	0.5	4.7	3.1	4.5	< 0.5	< 0.5
2: MPLP553	Bleached	0	80.5	6.0	0.9	< 0.5	4.7	2.3	4.8	nd	< 0.5
2: MPLP552	Bleached	−50	79.9	6.1	1.1	0.5	5.0	2.2	5.1	nd	< 0.5

[1] Undifferentiated kaolin group minerals.
[2] Undifferentiated mica species including muscovite, biotite, illite, and illite–smectite; nd, not detected.

samples taken either side of a horizontal bleaching contact in Entrada Sandstone not immediately adjacent to a mineralized fracture. Iron content in the red sandstone is significantly higher (average 1.20 ± 0.05 wt% Fe_2O_3; 0.84 ± 0.04 wt% Fe) in the red sandstones than it is in the bleached sandstone (average 0.94 ± 0.03 wt% Fe_2O_3; 0.66 ± 0.02 wt% Fe). These values are in agreement with published values from a similar profile in the study area (Wigley et al. 2013).

Bulk Mineralogy: Quantitative XRD Data

Similar mineralogies at two sites associated with bleaching contacts in the Entrada Sandstone are shown in Table 3. Samples from profile Y are across a horizontal bleaching contact associated with the regional bleaching (Fig. 3) whilst the other set is from the vertical bleaching contact site associated with the site 2 mineralized fracture (Fig. 4). Quartz (78–82 wt%) is dominant with subsidiary carbonates (6–8 wt%), feldspars (5–7 wt%), and clay minerals (mica and kaolin groups combined, 4–6 wt%). Carbonates include calcite and dolomite in similar amounts, with dolomite marginally the more abundant of the two (3.9 to 5.1 wt% dolomite, 2.2 to 3.7 wt% calcite). Potassium (K–) feldspar is the dominant feldspar type (4.9 to 6.1 wt%); albite is a minor constituent (< 1.1 wt%). Hematite is the only mineral that shows a significant difference between the red and bleached sandstones, being non-detectable in the latter, present in minor amounts in the former. All other minerals, at both sites, do not vary across red and bleached sandstone contacts beyond the uncertainty in their quantifications; this is illustrated for profile Y in Figure 3 and for site 2 in Figure 4.

Petrography

The samples of Entrada Sandstone examined in this study are dominantly moderately to moderately well sorted, very fine- to medium-grained, quartz-feldspar sandstones of moderate porosity (2–9 vol%, from thin-section modal analysis; see supplemental material). Bedding is defined by variations in grain size, sorting, and locally by intergranular clay content. Grains are dominantly of quartz, with lesser feldspar (mostly K-feldspar with minor albite and other sodic plagioclases), scattered lithic fragments, and minor to trace mica flakes and heavy minerals (zircon, iron and titanium oxides, apatite). Some samples outside the immediate fracture sites but within the study area have low clay contents and are better-sorted, coarser-grained sandstones.

Intergranular clays are widespread, locally as a matrix in thin bed-defining laminae, more commonly patchily to generally dispersed. Clays are also present in scattered grain-sized aggregates, some with concentrically layered internal structures and varied silt contents. These clay pellets are locally preferentially compaction-deformed. Many sand grains have clay coatings; these are of varied thickness. In unbleached samples, the red color is hosted predominantly in the intergranular and grain-coating clays. Hematite, identified by XRD only in red host-rock samples, is the most likely coloring agent, and is rarely directly observable by SEM in the grain-coating clays.

Carbonate minerals, both calcite and dolomite, are common. Dolomite is typically slightly more abundant. Both carbonate phases are present in framework patches. These commonly contain rounded cores with turbid and angular internal textures visible under CCI and filtered SEM-CL imaging, and/or have non-luminescent cores under cold-cathode CL. Some of these cores contain silicate inclusions. The framework patches locally have a lamination control on their abundance. Carbonates are also present as widespread intergranular cements, associated with some clay-rich grains and partially to completely occluding secondary pores. Internal zoning textures are identifiable by a range of OM and SEM imaging techniques. EDXA shows that some zones are associated chiefly with variations in iron (Fe) content, particularly those in dolomite. Most of the internal zoning is in the form of concentric euhedral forms. Dolomite contains at least one zone with an irregular embayed outline. Where dolomite and calcite occur together, they are commonly intergrown. Each carbonate phase encloses aspects of the other, but whereas some calcite encloses dolomite with complete zone sets, dolomite only ever encloses partial calcite zone sets.

Evidence for detrital-grain dissolution is widespread and mainly of feldspars and lithic fragments, identified from grain remnants. There are two categories of secondary pores: one where the secondary pore has been significantly modified by compaction, the other where the secondary pore has not been modified by compaction. A high proportion of the latter contain cores of albite and are outlined by remnant clay rims or enclosing cements. Dolomite and calcite partially occlude both types of secondary pores.

Grain-coating and intergranular clays are dominantly illitic, based on SEM-EDXA and XRD. Kaolinite is a widespread intergranular and grain-replacive diagenetic phase. Quartz, albite, and titanium oxide are minor diagenetic phases. Diagenetic quartz is present mainly as minor partial overgrowths. Rare pyrite is present as fine euhedral intergranular crystals, but notably hosted only in bleached sandstone. A bituminous phase is
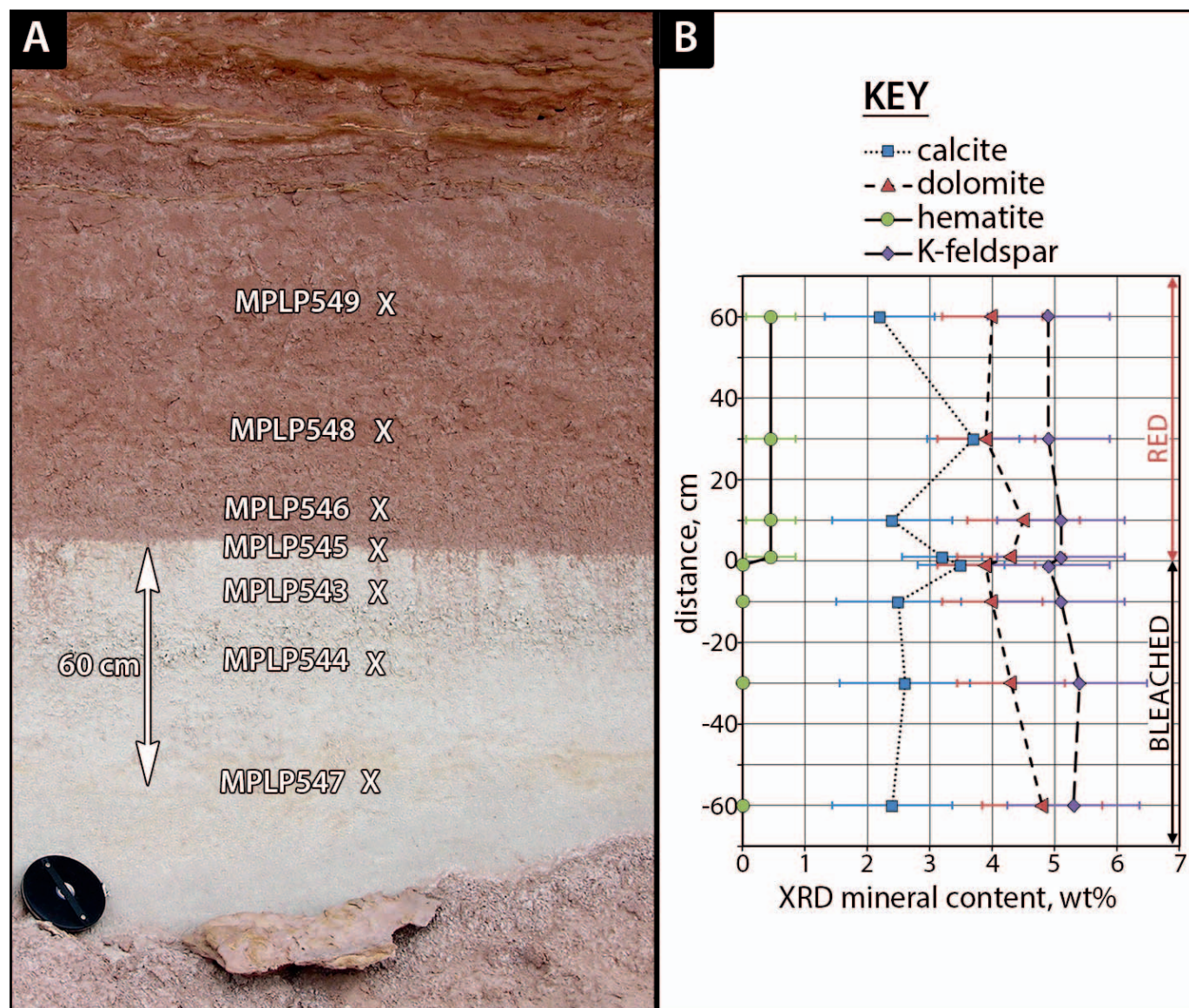
Fig. 3.—Sample site Y field photo and XRD-derived selected mineralogy profile. **A)** Field site photo for site Y (location shown in Fig. 1B) with an overlay of sample points. The bleaching contact is virtually horizontal in a bed of the Entrada Sandstone that shows little structure and is capped by a thinly horizontally bedded clay-rich unit. **B)** Plot of the XRD-derived quantitative mineral content data for the sample sites shown in A, showing the trends for selected minerals across the bleaching contact. Only hematite content varies significantly across the contact.

present as a pore-filling and pore-lining phase in samples of bleached sandstone from the east of the study area stratigraphically below and within 10 m of the horizontal bleaching contact.

Comparison of Bleached and Unbleached Sandstones

The pattern of "bleaching" of the host sandstones in the study area away from the fracture sites is not fully described here, but a brief summary of key observations is provided for context. As detailed above, total iron is lower in bleached samples than it is in red samples (Table 2). Additionally, hematite is undetectable in the bleached samples, whilst being a minor phase in the red samples (XRD bulk-rock analysis, Table 3). However, inside a particular bed set, other mineral contents are identical either side of the bleached–unbleached contacts, within analytical uncertainty (XRD data, Table 3, modal analysis, see supplemental material). Notably, total

carbonate, calcite and dolomite contents are as variable within the red and bleached zones as they are between them (Figs. 3, 4).

Petrographic observations are in agreement with the XRD bulk data; hematite has a detectable systematic difference in content across the bleaching contacts, whilst most other minerals do not. At non-fracture locations, where the contact is horizontal, pyrite was detected only in the bleached sandstone, where it is present in trace amounts (see supplemental material). Textural characteristics (grain size, sorting, compaction) are not systematically different immediately either side of the contacts, although the bleaching contact can coincide with bedding features such as clay-rich laminae. The complex internal textures of the intergranular carbonate cements are similar on both sides and specifically immediately either side of the contacts. Modally-derived carbonate abundances on a fine (mm) scale (from SEM X-ray mapping phase modal analysis) are again as variable within the red and bleached zones as they are between them (see
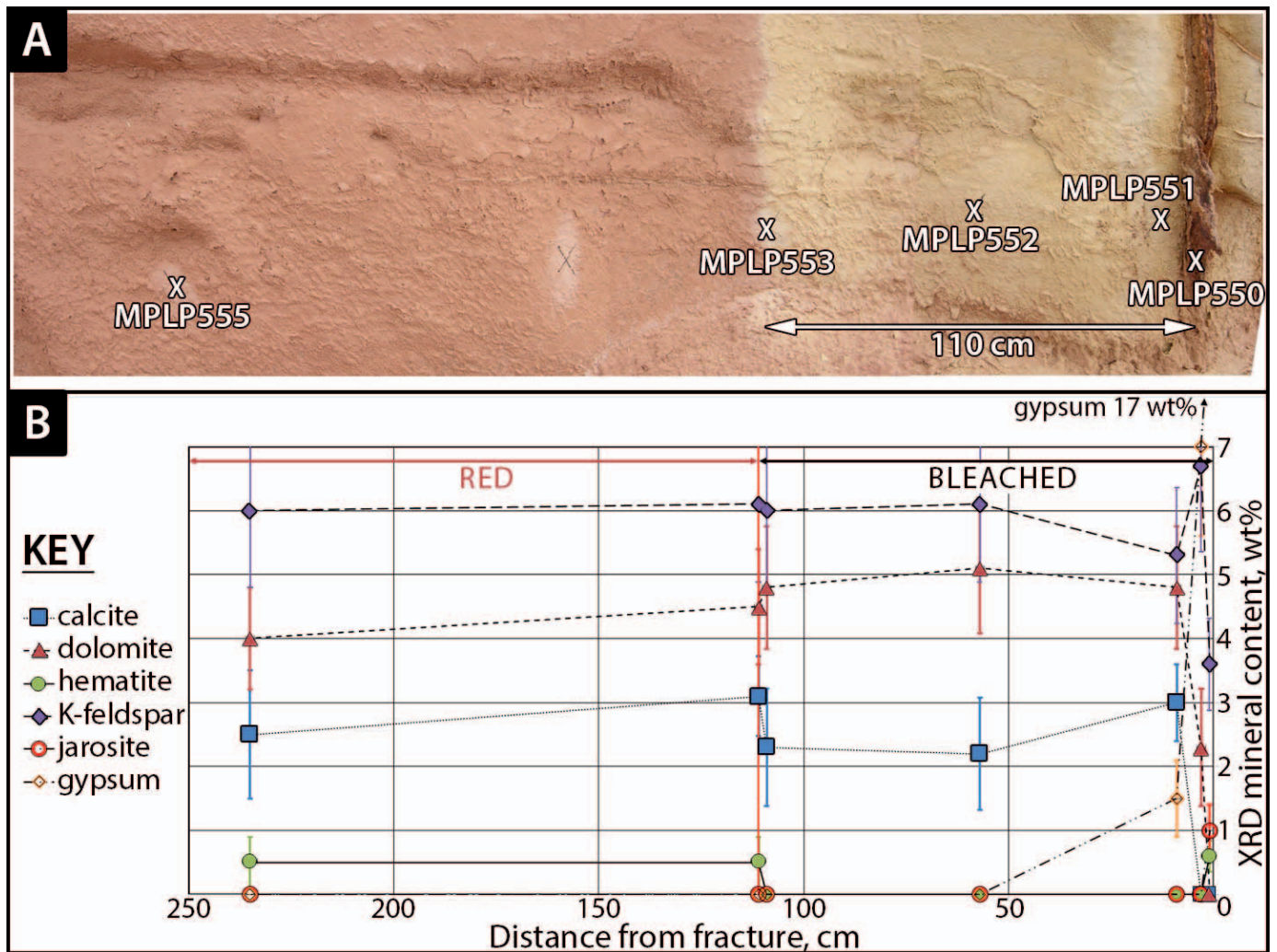
F$_{IG}$. 4.—Sample site 2 field photo and XRD-derived selected mineralogy profile. **A)** Field site photo for site 2 (location shown in Fig. 1B) with an overlay of sample points. Sample location MPLP550 included both fracture mineralization and material from the adjacent bleached wall rock and sample site MPLP553 was split into bleached and unbleached portions. The bleaching contact is essentially vertical, subparallel to the fracture, in a bed of Entrada Sandstone with poorly defined horizontal bedding. **B)** Plot of the XRD-derived quantitative mineral-content data (full dataset in supplementary data) for the sample sites shown in Part A, showing the trends for selected minerals across the bleaching contact, and within and adjacent to the mineralized fracture. Only hematite content varies significantly across the bleaching contact. Gypsum is present only near to the fracture and reaches a maximum in the fracture. Calcite is absent and dolomite depleted in the wall rock; both are absent in the fracture. Jarosite is detectable only in the fracture. More detailed fracture mineralogy is also given in the supplemental material.

supplemental material). Other diagenetic phases, such as kaolinite, also have similar abundances and modes of occurrence either side of the contacts. Similarly, secondary porosity shows no significant difference in amount or type across bleaching contacts.

RESULTS: FRACTURE-ZONE MINERALOGY AND PETROGRAPHY

Field Observations

The three fracture sites described here are composite fractures. At each, the main fracture comprises several nested, parallel and subparallel, fractures with varied types and degrees of mineralization (Fig. 2D, F). Some fractures bifurcate. At some locations (particularly site 2) there are fine, oblique fractures with white fill that crosscut the main fracture, but that are also displaced by some elements of it. The main fracture fills are deep red, ochre, and white (Fig. 2D, F), although not all types are present at every fracture site. The host rock is bleached either side of the fracture on a centimeter (Fig. 2F) to meter (Fig. 2A, C, E) scale. At some

locations, some crosscutting fractures with white fills have no associated bleaching. Ochreous and, to a lesser extent, deep red colors are present in the otherwise bleached host sandstone within and immediately adjacent to the fracture zones (Fig. 2D, F). The ochreous color is typically strongest at the fracture centers, and fades with increasing distance from the fracture centers over distances of 1–10 cm (Fig. 2D, F). Some fractures with white fills crosscut the deep red and ochreous mineralizations. Additionally, at some locations there are divergent white-filled fractures that do not have any of the red and/or ochreous coloration (Fig. 2D).

XRD-Derived Fracture and Wall-Rock Mineralogy

XRD characterization shows that the major mineral phases associated with the fracture mineralization are goethite, hematite, jarosite (KFe₃(SO₄)₂(OH)₆), and gypsum (Fig. 5, Table 4 and XRD see supplemental material). Subsampling of individual fractures and associated color bands
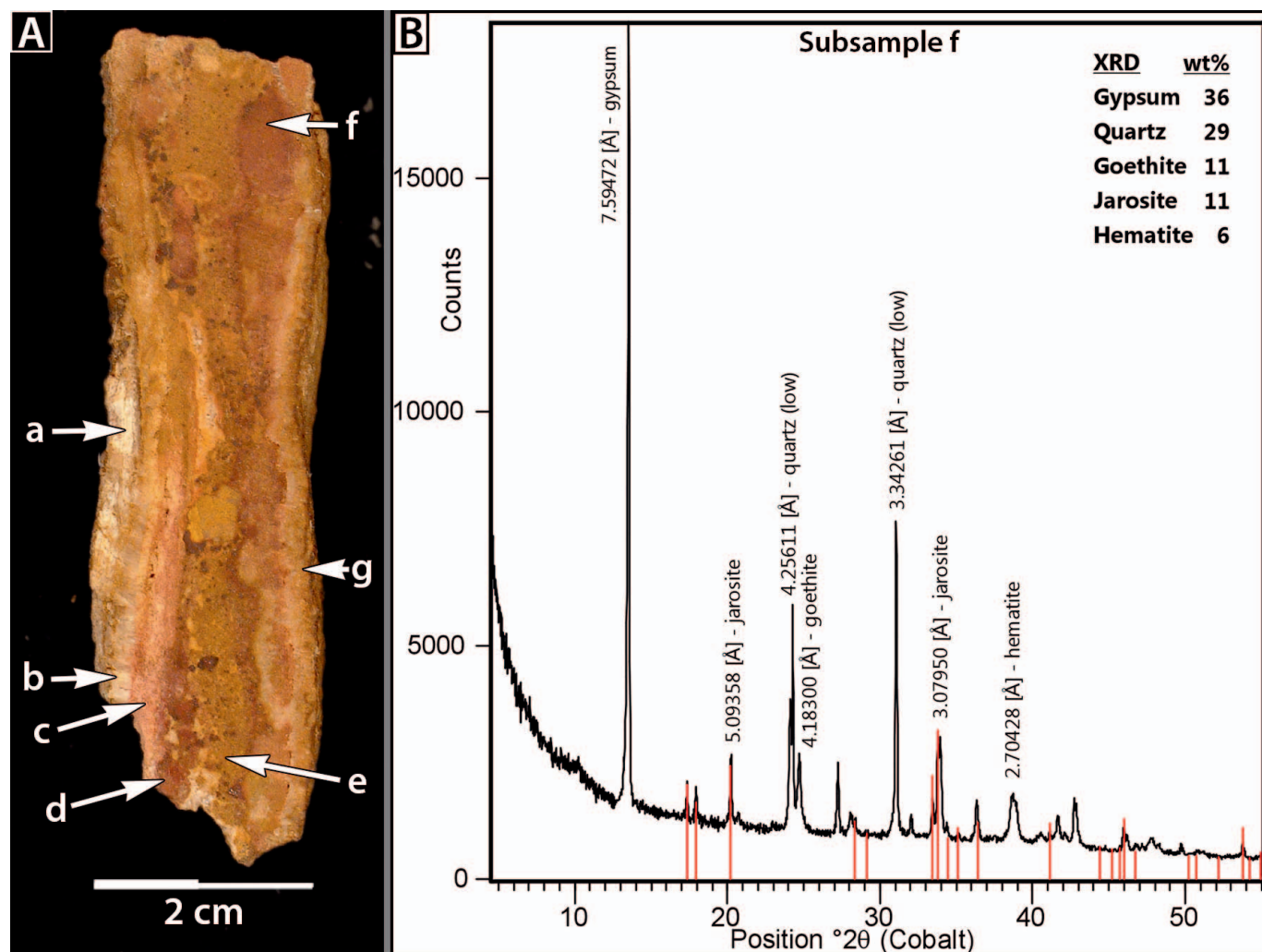
J.C. RUSHTON ET AL.

Fig. 5.—Site 3 fracture sample with XRD analysis subsample locations and derived XRD data. **A)** Photo of the mineralized fracture sample (MPLP599) showing the locations of sites of semiquantitative XRD analysis subsamples; results are shown in Table 4. Sites selected are different color zones and fractures. **B)** XRD trace from subsample site f, as marked in Part A, with the peaks of major mineral phases labelled and quantified. Stick-pattern overlay is for jarosite.

shows that the variations in color are associated principally with differing proportions of these minerals, with the ochreous zones typically being rich in goethite, whilst deep-red zones additionally contain abundant hematite (Table 4). Rare fractures contain detectable pyrite (e.g., site 1 fracture mineralization; XRD see supplemental material), and these are also highly enriched in hematite and goethite. XRD analysis shows that the white fills of both the main and crosscutting fractures are mostly of gypsum. Some are cemented predominantly by calcite (Table 4; Fig. 5, feature a).

TABLE 4.—*Semiquantitative XRD data for subsamples taken from the mineralized fracture sample (MPLP599), site 3, as shown in Figure 5.*

		Silicates				Carbonates		Sulphates		Others	
		Quartz	K-feldspar	Kaolin[1]	Mica[2]	Calcite	Dolomite	Gypsum	Jarosite	Hematite	Goethite
Subsample	Subsample Location Description					weight %					
a	White fracture cement	5	4	nd	2	86	nd	3	nd	nd	nd
b	Gray, cross-fiber fracture cement	5	nd	nd	1	1	nd	93	nd	nd	nd
c	Pale red wedge	64	7	1	2	2	nd	17	8	nd	nd
d	Patchy dark red intermixed with white	34	5	nd	1	nd	nd	48	3	3	6
e	Broad irregular buff band	35	7	< 1	3	nd	nd	52	nd	nd	2
f	Patchy dark red	29	4	< 1	3	nd	nd	36	11	5	11
g	Pale orange, cross-fiber fracture cement	19	7	nd	nd	nd	nd	68	nd	nd	6

[1] Undifferentiated kaolin group minerals.
[2] Undifferentiated mica species including muscovite, biotite, illite and illite–smectite; nd, not detected.

Calcite and dolomite are absent or depleted (compared to the host rock) in a thin zone of the wall rock (on a millimeters to centimeters scale) adjacent to jarosite-mineralized fractures (Fig. 4B), whilst gypsum is a common additional phase even outside the white-cemented fractures (Table 4; Fig. 5, features c–f).

Definitive jarosite identification by XRD (Fig. 5) enables its identification by SEM and OM in other samples from comparative imaging, compositional (EDXA), and optical properties.

Wall-Rock Petrography

Textural disruption of sedimentary bedding associated with the fractures takes a number of forms. At two sites the disruption is such that the bedding structure of the sandstone has been lost over centimeter-scale thicknesses (sites 2 and 3). At site 1 the bedding is retained with millimeter-scale vertical displacement.

At each of the three sites investigated, host-rock carbonates are absent from the wall rock directly adjacent to jarosite-bearing fractures, to a thickness of up to 1 cm. Beyond this zone, there is a progressive increase in the content of carbonates to 2–3 cm from the fracture zone, after which the abundance and distribution of carbonate is similar to that of the host rock (Fig. 6B). In the transition zone between these extremes, carbonates are present as small patches partially occluding open pores (Fig. 6A), some with embayed margins, and dolomite is present closer to the fracture than is calcite. Rare euhedral carbonates are of calcite, and these, under CL and CCI imaging, show internal structures of anhedral cores with irregular, embayed and jagged margins, with the final, euhedral, zone typically brightly luminescent under CL.

Gypsum cementation in the wall rock is typically present with an abundance inverse to that of the carbonates. Minerals tentatively identified in trace amounts in this zone, based on qualitative SEM-EDXA compositions, include svanbergite ($SrAl_3(PO_4)(SO_4)(OH)_6$), glauberite ($Na_2Ca (SO_4)_2$), and goyasite ($SrAl_3(PO_4)(OH)_5.H_2O$).

Fracture: Rock Mineral Assemblages, Relationships, and Textures

Site observations and mineralogical analysis reported above show that there are two main types of fracture present at all three study sites identifiable by their physical appearance, and their mineral assemblages and relationships:

I. Those that are dominantly mineralized by iron-rich phases: these contain single or multiple parallel bands of red-brown to ochreous phases (Figs. 2C, 5A) comprising some or all of goethite–hematite–jarosite (Table 4, Fig. 5, see supplemental material) which are bounded by bleached host rock.

II. Those that are cemented by calcium-based phases: their fill is typically white at outcrop and comprises gypsum and/or calcite. Bleaching patterns do not follow these fractures, although they can be contained within bleached areas. The calcium-based fractures can be seen to run both parallel with and crosscutting the iron-based fractures in the field.

The iron-rich mineralization, when observed and analyzed by SEM and OM techniques, itself has two main textural forms that are typically concomitant:

a) Highly concentrated bands with low sand-grain contents (Figs. 6C, D, 7A) and 20–60 wt% (XRD) iron-rich phases.

b) Zones and bands of iron-bearing phase enrichment within texturally disrupted sandstone (Figs. 6C, D, 7D).

Highly Concentrated Bands of Iron-Rich Mineralization.—These are patchy, optically opaque, dark brown, ochreous brown, and dark green

(Fig. 6C, D). Definitive identification of jarosite by XRD (Fig. 5) informs and confirms the identification of jarosite from EDXA-derived elemental compositions in these bands (Fig. 7B). This, in turn, shows that green areas are those which are jarosite-rich (Fig. 6C, D; compare with Fig. 7A, B). By contrast, whilst XRD shows that goethite and hematite are commonly present together, they are difficult to separate by microscopic techniques. Identification of these iron phases as an unresolved mix (henceforth termed iron oxide–hydroxide) is, however, straightforward from EDXA-derived compositional characteristics. Comparison of this SEM-derived compositional data with optical microscope observations shows that the areas with the highest concentrations of iron oxide–hydroxide are those which are optically opaque, dark brown, and ochreous brown.

There are complex intergrowth textures of iron oxide–hydroxide and jarosite in the concentrated iron-rich bands. The jarosite is present as packed microcrystals in rounded (Fig. 7A), elongate (Fig. 7C), and equant euhedral (Figs. 7A, 8A) forms. These "domains" of jarosite are variably porous. The iron oxide–hydroxide is present around the margins of the jarosite, defining domain margins (Fig. 7A, C). The iron oxide–hydroxides are also present in low-jarosite and jarosite-free concentrations with rounded, irregular, and radial textures, locally with concentric zone patterns. As with the jarosite, equant blocky and euhedral forms are widespread. Some of the more porous jarosite domains contain fine (10–30 μm) blocky crystals of iron oxide–hydroxide (Fig. 7C). Sparse sand grains and angular grain fragments (almost entirely quartz) are commonly constrained to the material between jarosite domains (Fig. 7A, C). Elongate jarosite domains are present in slightly splayed subparallel clusters perpendicular to the iron mineralized fracture (Fig. 7C).

A prominent feature common to all three sites is the presence of equant blocky to euhedral forms in the highly concentrated bands. These occur on a scale of 50–200 μm and comprise either iron oxide–hydroxide or jarosite outlined by iron oxide–hydroxide (Figs. 7A, 8A). The euhedral forms typically define quadrilateral or triangular shapes with truncated edges and apices (Figs. 7A, 8A, B) that are suggestive of a cubic habit. This interpretation is supported by the identification of clusters of interlocking equant blocky iron oxide–hydroxide cubic forms in a rock chip sample from the site 3 fracture mineralization (Fig. 8D), with truncated apices and striated edges. Jarosite, hematite, and goethite do not form with a cubic habit. Embayed and fractured pyrite, which is a cubic mineral, is present in some of these cubic forms at site 1 (Fig. 8C).

Quantitative EDXA analysis of the iron oxide–hydroxide in these forms (see supplemental material) mostly give analytical totals close to those expected from goethite and lepidocrocite (stoichiometrically calculated oxide totals up to 91 wt%, assuming all iron is present as Fe^{3+}; ideal FeOOH has a total of 90 wt% Fe_2O_3), consistent with identifications from XRD analyses. There is considerable variation in analytical totals associated with some of this mineralization, with the lower totals typically coinciding with lower backscatter coefficients. This potentially reflects variations in micro-porosity or water content of the iron alteration products: it is likely, therefore, that these materials comprise a mix of variably hydrated iron oxide–hydroxides, some cryptocrystalline and/or amorphous. Hematite is rarely distinguishable in section, but its widespread presence is indicated by XRD, suggesting that it too is intermixed with the other iron-based constituents.

Quantitative EDXA analyses of the pyrite in the centers of some of these equant forms (see supplemental material) show that they mostly contain significant arsenic (up to 3 wt% As). The adjacent iron oxide–hydroxide constituents also contain significant arsenic, in varied amounts and up to 5 wt%. Arsenic is also detectable in some of the jarosite patches as well as the more widespread network iron oxide–hydroxide deposits at all three sites.
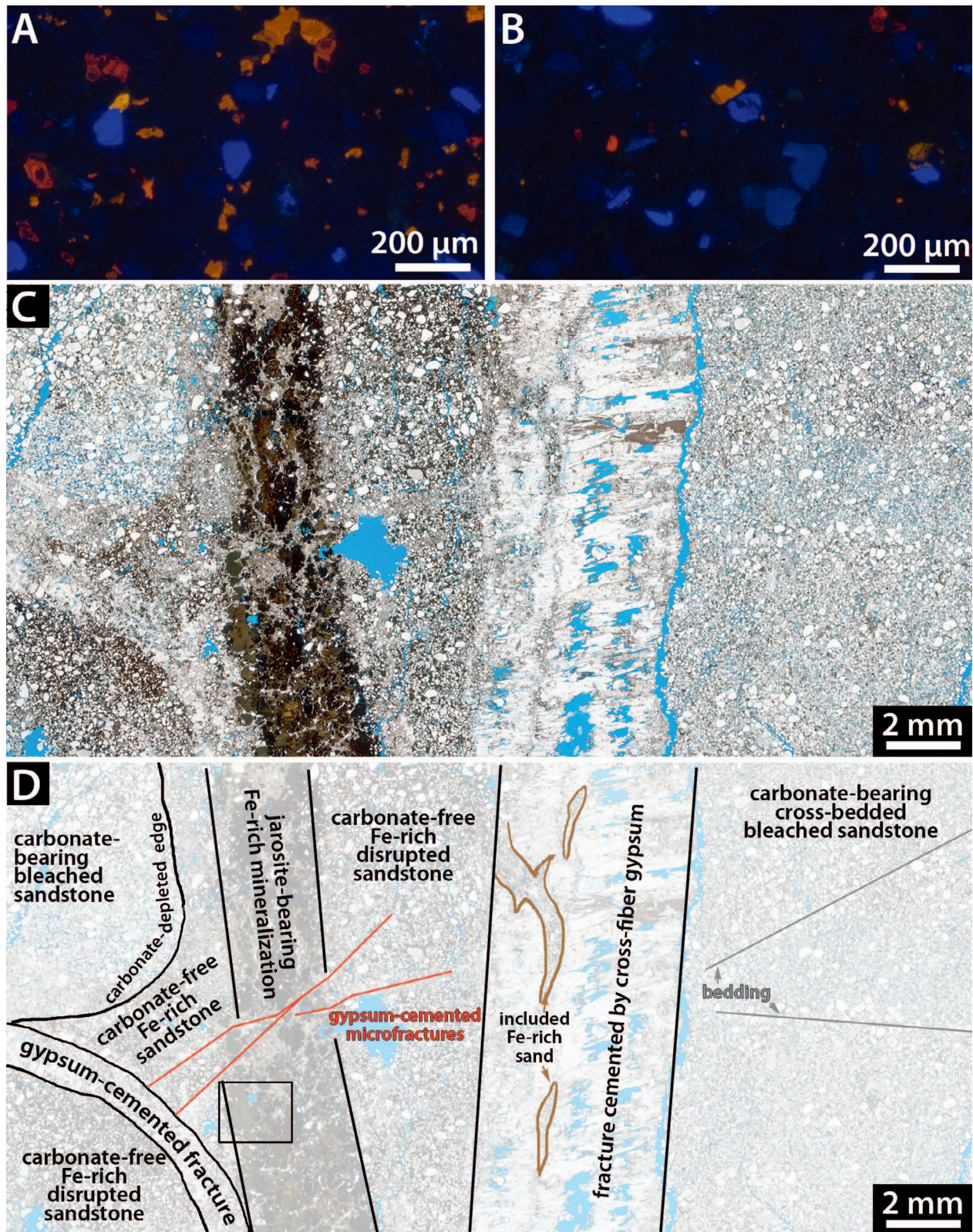
Fig. 6.—**A)** CL image from a site 2 sample taken approximately 10 cm from the mineralized fracture, showing a content and distribution of carbonates (calcite, yellow orange; dolomite, red orange) that is typical of samples more distal from fractures as well as of unbleached sandstone. Blue luminescent grains are K-feldspar. **B)** CL image from a site 2 sample proximal (< 1 cm) to the mineralized fracture, for comparison with Part A, showing much reduced carbonate content. **C)** An image under transmitted light of a polished thin section from site 1 (sample MPLR916A). Blue areas show porosity. **D)** Marked-up version of Part C, highlighting key features (phase identifications from optical, SEM EDX, and XRD analyses). To the left is an example of a fracture rich in iron-based mineralization, with a blocky opaque to sub-opaque fill; this contains jarosite in addition to goethite, hematite, and gypsum. Boxed area is the site of Figure 7A. The cross-fiber texture (Ramsey 1980) and lines of inclusions in the main gypsum-cemented fracture are both indications of episodic gypsum growth with contemporaneous opening. Gypsum also cements oblique microfractures that cut the iron-rich fracture and the curved fracture that cuts adjacent iron-rich sandstone.
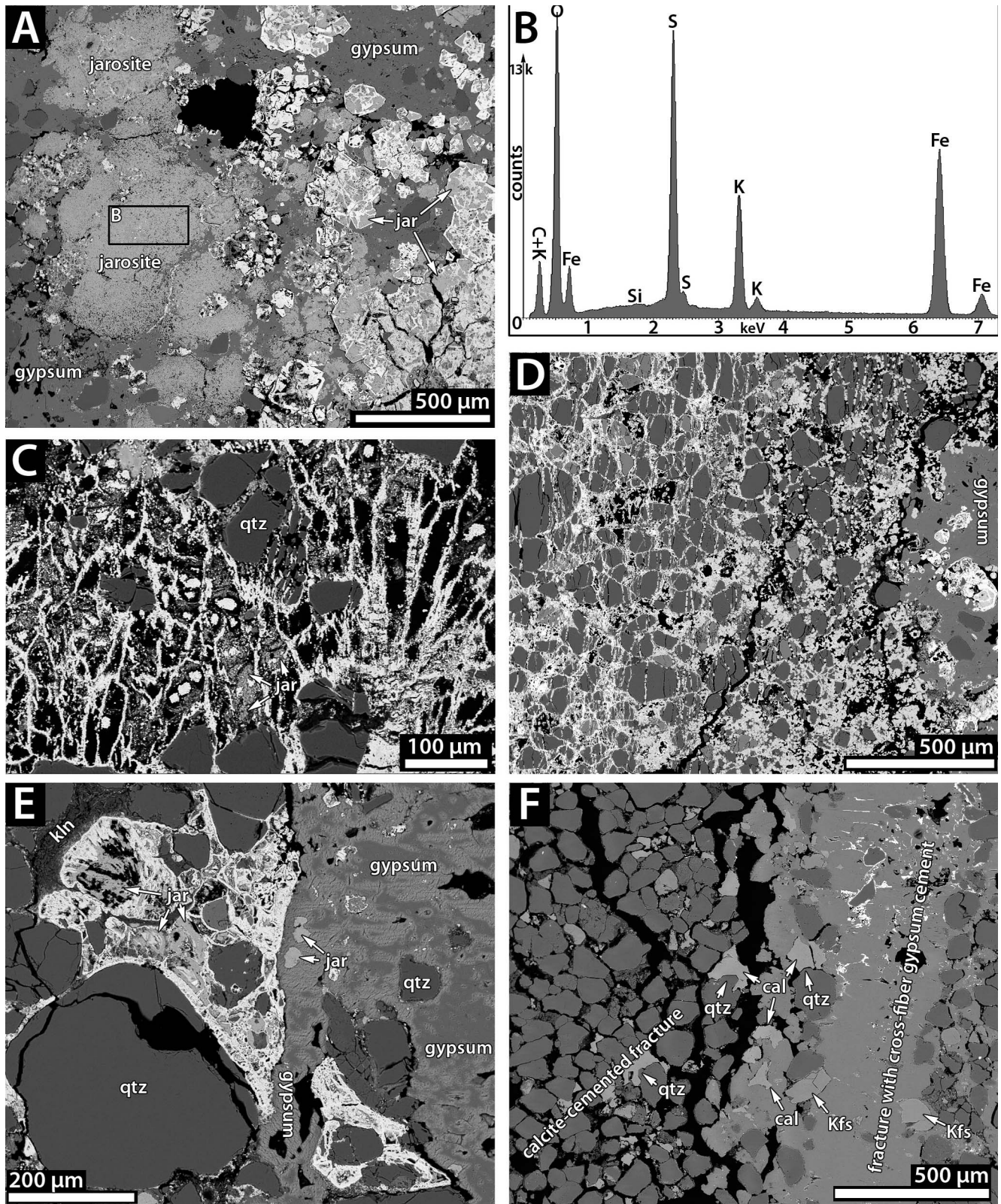
FIG. 7.—Parts A and C–F are BSEM images from polished thin sections. **A)** From the boxed area in Figure 6D (a site 1 sample), showing the textures and mineralogy of the iron-rich mineralization. A band of euhedral to granular forms outlined in high brightness iron oxide–hydroxide runs down the center-right part of the image and many of the outlined forms have jarosite (jar) fill; these are interpreted as pyrite pseudomorphs (see Fig. 8). Jarosite is additionally present as fracture fill in bulbous aggregates (left); these correspond to dark green areas in Figure 6C. Gypsum is a widespread enclosing and infilling (i.e., later) cement. Quartz grains are sparsely distributed. **B)** An SEM-EDX spectrum taken from the boxed area in Part A showing a composition consistent with the identification as jarosite (C comes from a carbon coating). **C)** This shows textures in
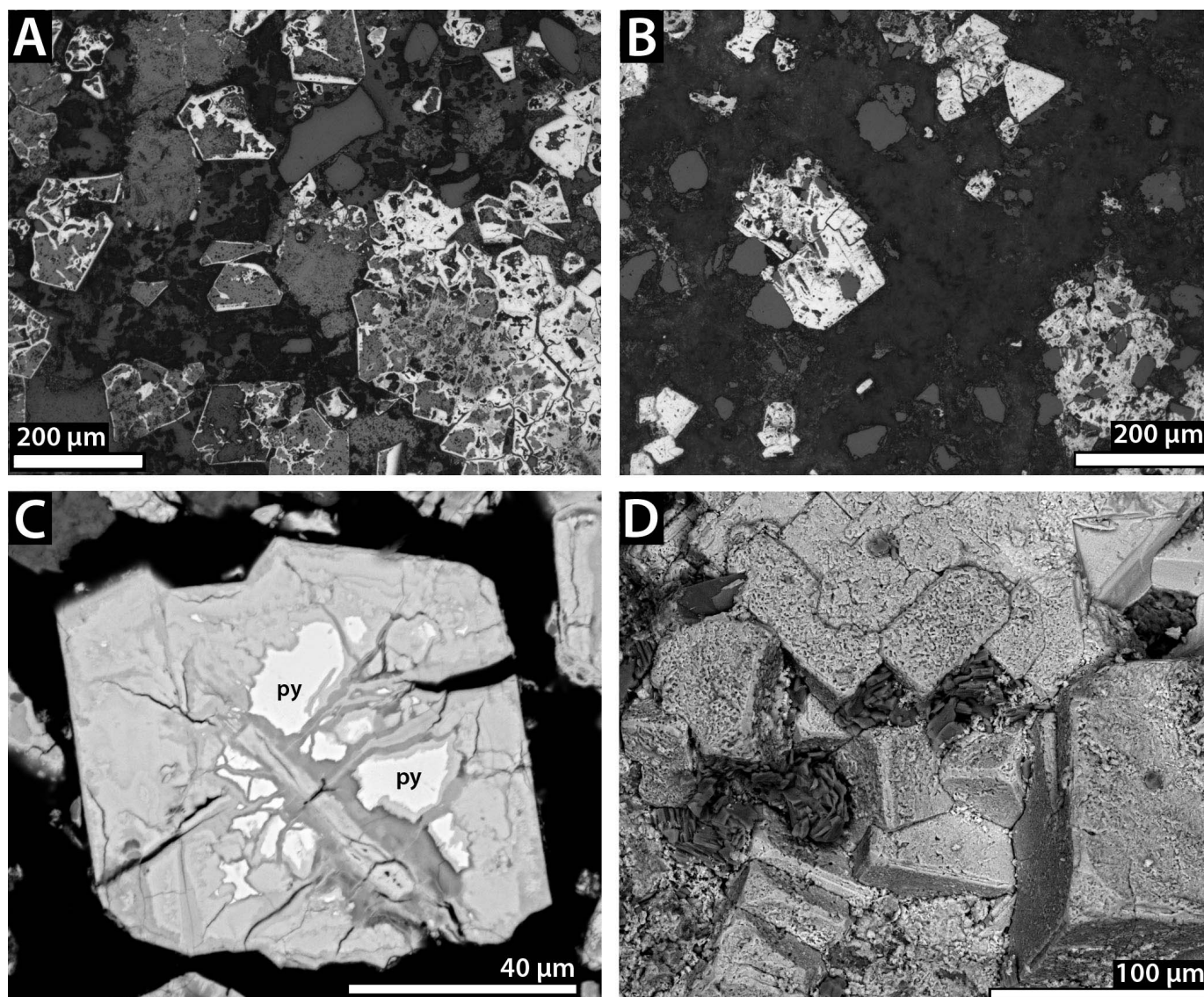
Fig. 8.—BSEM images illustrating the presence of pyrite and its likely pseudomorphs in the concentrated iron-rich parts of the fracture mineralizations; Parts A–C are from polished thin sections. **A)** (Site 1) shows polyhedral forms outlined in high-brightness iron oxide–hydroxide. Various quadrilateral and triangular shapes are consistent with cross sections of cubic crystal forms. The darker infill to the outlines is predominantly of jarosite. **B)** (Site 3) shows similar forms defined predominantly by high brightness iron oxide–hydroxides. **C)** (Site 1) shows an equant blocky form, comprising iron oxide–hydroxide, in this case containing embayed and fractured pyrite (py) remnants. The pyrite and surrounding phase both contain arsenic (see supplemental material for quantitative microanalysis data). **D)** (Site 3) is a rock-chip sample and shows a cluster of interlocking cubic forms with the truncated apices and striated edges typical of the cubic habit in general. They are formed of iron oxide–hydroxide. This is a morphology commonly seen in diagenetically formed pyrite.

←

a site 2 sample associated with part of the central mineralization assemblage. The high brightness phase, which is iron oxide–hydroxide, outlines elongate forms. Elongation is approximately perpendicular to the fracture orientation. Sand grains are floating and some that are fractured show "trails" parallel to the elongation. Whilst some of the elongate forms are now porosity, many are filled or partially filled by jarosite. Some of the partially filled domains also contain equant crystals of iron oxide–hydroxide. **D)** Shows an area from a site 1 sample of iron-rich texturally disrupted sandstone; grains are fractured nearly parallel to the central fracture (gypsum-cemented pyrite pseudomorphs at right edge). Iron oxide–hydroxide (high-brightness phase) cements fractures and intergranular pores. **E)** From a site 1 sample, on the left is iron-rich disrupted sandstone, comprising quartz (qtz) grains and intergranular kaolinite (kln) cemented by iron oxide–hydroxide (high brightness) and jarosite (jar). This has been fractured, and the gypsum fracture cement encloses fragments of the iron-rich sandstone (lower right) as well as floating quartz and jarosite. **F)** From a site 1 sample, showing a weakly defined calcite-cemented fracture intersected by a gypsum-cemented fracture with a cross-fiber texture. The gypsum has included some detached sand grains (including K-feldspar, Kfs) and calcite (cal), showing that at least some of the gypsum postdates the calcite. Quartz grains bounding the calcite show preferential developments of quartz overgrowths (qtz).

Areas Enriched in Iron-Bearing Phases Cementing Texturally Disrupted Sandstone.—These are commonly developed in the rock adjacent to the highly concentrated bands (Fig. 6C, D) and are cemented by a mix of iron oxide–hydroxides and jarosite, with common and locally dominant gypsum. Common textures in this material are of sand grains surrounded by cement. Grains are commonly fractured, and the fragments separated, particularly immediately adjacent to the main fractures (Fig. 7C, D). Grain-fracture orientation and separation are respectively predominantly parallel, and nearly-perpendicular, to the orientation of the main fractures (Fig. 7D). Locally, detrital-grain separation is associated with elongate forms outlined by rims of Fe oxide–hydroxide (Fig. 7C) with shapes that are oriented perpendicular to adjacent iron-mineralized fractures. Sand grains are floating, and some that are fractured have grain fragment "trails" parallel to the elongation. The elongate forms outline porosity, jarosite, and fine equant crystals of iron oxide–hydroxide. Gypsum is present as patchy cement enclosing the other constituents.

Fractures with Calcium-Based Mineral Fill.—These comprise gypsum- and calcite-cemented veins that run parallel to and crosscut the iron-based mineralization. These relationships are apparent at outcrop, hand-specimen, and microscopic scales (Figs. 2D, 6C, D). Coarser gypsum veins (millimeter to centimeter scale) typically have antitaxial cross-fiber textures (Fig. 6C, D; using the terminology of Ramsay (1980)). These vein fills also contain bands of inclusions of sand grains (Fig. 6C) and, where gypsum-cemented fractures intersect iron-based mineralization, fragments of the iron-rich phases (Fig. 7E), as well as slivers of cemented, disrupted sandstone (Fig. 6C, D). There are scattered fragments of calcite, enclosed within the gypsum, which have sizes and shapes similar to the vein calcite (Fig. 7F).

The calcite-cemented veins comprise predominantly coarse interlocking calcite that has concentric CL-resolvable growth zoning associated with variable trace manganese content (as detected by SEM-EDXA). Some have sigmoidal forms. This calcite is texturally different from the carbonate cement observed in the host rocks, described above. It is the only carbonate present at fracture centers and the immediately adjacent wall rock where the host rock carbonates are absent (Fig. 7F). Quartz overgrowths are notably better developed at the margins of the calcite-cemented fractures than elsewhere in the fracture assemblages, wall rocks, or host rocks (Fig. 7F). Some gypsum veins contain inclusions of calcite and quartz grains with these better-developed overgrowths, showing that at least some fracturing and gypsum mineralization postdates the calcite-quartz overgrowth assemblage (Fig. 7F).

DISCUSSION

Host-Rock Petrography

The study area Entrada Sandstone displays textures and features that fit well with the regional depositional model proposed for the Entrada Sandstone, as an example of a wet dune system (Crabaugh and Kocurek 1993). Clay-poor sandstones typical of "clean dune" eolian deposits were encountered in this study, but more commonly samples were of the type with patchy intergranular clays, enriched as a matrix in some thin laminae. This clay distribution is typical of damp interdune deposits, as are some grain-coating clays, interpreted as inherited clay rims on the basis of their varied thickness and surface-parallel orientations (Wilson 1992).

The carbonate minerals are of key interest; these are present in the host sandstone, as a cement to some fractures, and are also notable by their absence in some parts of the fracture and wall rocks. Carbonates have been shown to react readily with CO_2-bearing fluids, so are a key "indicator" mineral group when looking for evidence of such reactions (Rochelle et al. 2002; Weibel et al. 2014). Combined CL, CCI, and BSEM imaging reveals

that the carbonates have a complex paragenesis. The grain-like non-luminescent (by CL) cores of framework carbonate patches are interpreted to have detrital or syndepositional origins as carbonate "micro-concretions." This origin is suggested by the location of the cores as part of the sandstone framework combined with their concentration along some laminae. Additionally, the observed turbid and angular core textures are consistent with pedogenic and evaporative origins, processes expected in the arid wet-dune sedimentary setting of the Formation (Kocurek 1981; Crabaugh and Kocurek 1993; Garden et al. 2001). Carbonates with similar origins have been identified in the underlying Navajo Sandstone (Parry et al. 2009), which likely formed under similar depositional conditions. The identified widespread clay-rich pellets and rare carbonate-cemented intraclasts further support this interpretation, being consistent with localized reworking of hard crust or pedogenic materials.

Following the terminology of Schmidt and McDonald (1979), mesodiagenetic carbonate formation, commonly extending from the eodiagenetic micro-concretions, has occurred episodically, as shown by the concentric CL-resolved zoning in both calcite and dolomite. An episode of dolomite dissolution is also revealed by CL. A key observation taken from the study is that the carbonates show no significant differences in the carbonate contents, distribution, textures, or their paragenetic sequence either side of the bleaching contact. The evidence for dolomite dissolution is present on both sides of the contact. Neither carbonate dissolution nor precipitation can be associated with the bleaching event.

These observations are in contrast to those of Wigley et al. (2012), who report local concentrations of diagenetic carbonate cements at bleached–unbleached sandstone contacts, which they attribute to the bleaching event. No such concentrations were observed in our samples, which include both vertically and horizontally oriented bleaching-front contacts from several sites. We note, however, that their example image of this carbonate has some characteristics in common with what we have identified as eodiagenetic carbonate-cemented intraclasts.

Other key diagenetic events in the host rock are the dissolution of grains, particularly feldspars, and the formation of kaolinite. There are no significant differences in the abundance or distribution of these either side of the bleaching contact. The bleaching event has not resulted in an identifiable episode in the silicate diagenetic history either. The only detected difference between the bleached and unbleached host-rock both at, and distal to, fracture sites is in the hematite content (Table 3).

Pyrite Formation and Pyrite Oxidation

The key to understanding the paragenesis of the fracture mineralization is the recognition that the cubic forms, defined by clusters and intergrowths of non-cubic phases, are pseudomorphs of pyrite. The presence of pyrite remnants centered in some of these pseudomorphs at one site (Site 1, Fig. 8C) is principal evidence of the mineral's existence and replacement. Occurrences of similar pseudomorphic forms at the other fracture sites mean that pyrite existence and replacement can be inferred there too. The associated mineral assemblages further support this assertion. They are characteristically rich in Fe^{3+} oxides, oxyhydroxides, sulfates, and sulfate hydrates. Of particular note is the presence of jarosite $(KFe_3(SO_4)_2(H_2O)_6)$. Jarosite formation occurs in Fe^{3+}-rich, acidic (pH < 3), high-Eh (oxic) environments (Stoffregen et al. 2000; Zolotov and Shock 2005; Smith et al. 2006), and is most commonly found as a product of the oxidative alteration of sulfide minerals (Bladh 1982; Long et al. 1992 ; Bigham and Nordstrom 2000; Bell and Bowen 2014).

At each of the fracture sites examined in this study, pyrite was abundant at the center of the fracture, and this was at the center of fracture-associated bleaching. Our analyses show that the bleaching is associated with the removal of hematite and a decrease in the total iron content of the sandstone. The spatial association between pyrite and bleaching could

result from their contemporaneous development through the action of reducing fluids moving preferentially along the fractures, which were pathways of higher permeability, with the pyrite being a sink for the reduced iron. A number of different potential reducing agents, such as hydrogen sulfide (H_2S), organic acids, methane, and hydrocarbons, are commonly associated with hydrocarbon migration (Chan et al. 2000; Garden et al. 2001; Eichhubl et al. 2009), and bituminous deposits observed in the field in the Entrada Sandstone, at sites below the bleached fronts of the horizontal bleaching (Pearson, field observations; Wigley personal communication, 2012), are an indication of the previous presence of hydrocarbons in the rocks of the study area. Of these possible reducing agents, H_2S is a good fit for producing both pyrite and bleaching. Additionally, there are none of the coeval reaction products in the bleached zones that would be expected if other potential hydrocarbon-migration-related reducing agents had been involved (principally carbonates such as siderite and calcite; Chan et al. 2000).

Consequently, our hypothesis is that H_2S was the main reducing agent in the Salt Wash Graben area faults. It is likely that the H_2S was present in brines originating from hydrocarbon maturation and migration. This mechanism has been proposed as a potential bleaching mechanism by other studies in the nearby Moab Anticline region (Chan et al. 2000; Garden et al. 2001). The reaction suggested is

$$2H_2S + Fe_2O_3 + 2H^+ \rightarrow FeS_2 + 3H_2O + Fe^{2+} \qquad (1)$$
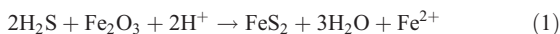
If we take the above pyrite-mineralization reaction, in combination with the observed 0.3 wt% decrease in Fe content in the bleached sandstone (Table 2), then a simple mass balance calculation can be made. The calculation requires the following assumptions and simplifications:

- The measured approximate 0.3 wt% loss of Fe in the bleached sandstone is due to the pyrite formation reaction (Equation 1)
- The reaction suggests that only half of the Fe loss will have gone into pyrite.
- 1 g of Fe will form approximately 2.1 g of pyrite.
- Pyrite and moderately porous sandstone have approximate densities of 5 g/cm^3 and 2.5 g/cm^3 respectively.

Using these, reduction of a 1 cm^3 block of sandstone would result in a 0.016-mm-thick layer of pyrite. A 2 mm thickness of pyrite, more typical for the observed thickness of the interpreted pyrite mineralization, would therefore require the bleaching of a 1.3 m thickness of sandstone, which is of a scale similar to field observations of bleach-zone thicknesses associated with the fractures, further supporting the hypothesis that H_2S was the dominant reducing agent involved in the bleaching.

We consequently propose that the formation of pyrite was initiated by the migration of highly reducing H_2S-bearing fluids. These fluids utilized fractures that were either pre-existing or that formed coevally with the fluid movement. Fe was liberated as Fe^{2+} from the reduction of Fe^{3+} minerals, principally the hematite contained in the grain-coating clays of the wall-rock sandstone, and then precipitated as pyrite as per the above reaction (Equation 1). The consequential Fe^{2+} concentration gradient between the fracture center and wall rock resulted in the increase of Fe in the fractures and a decrease of Fe in the wall rock. As the redox front moved farther into the sandstone wall rock, through either advection or diffusion, more Fe would have been liberated and moved down the concentration gradient to precipitate as pyrite in the fracture, widening the bleached zone until the H_2S was exhausted.
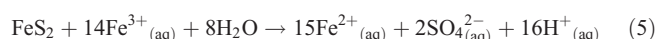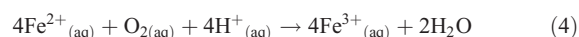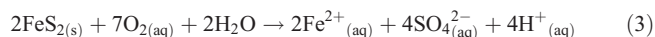
Petrographic evidence is clear that oxidation of the pyrite is the next diagenetic event recorded in the fractures. Notably, pyrite present in fracture-distal bleached host rocks has not been significantly oxidized, showing both that the oxidation event was not a surface weathering event and that the movement of the pyrite-oxidizing fluids was constrained to the fractures.

Pyrite oxidation is a complex process that comprises a number of different steps (Garrels and Thompson 1960; Singer and Stumm 1970; Bigham and Nordstrom 2000). This can be summarized by the overall equation

$$4FeS_{2(s)} + 15O_{2(aq)} + 14H_2O \rightarrow 4Fe(OH)_{3(s)} + 8H_2SO_{4(aq)} \qquad (2)$$
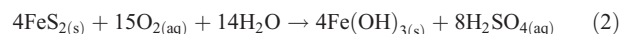
Both the Fe and S are oxidized. The generation of very low pH values by the process is implicit in the formation of sulfuric acid as one of the main reaction by-products. The use of $Fe(OH)_3$ is a generic indication of insoluble Fe III phases.

In reality, pyrite oxidation is a complex process that can be split into a series of steps:

$$2FeS_{2(s)} + 7O_{2(aq)} + 2H_2O \rightarrow 2Fe^{2+}_{(aq)} + 4SO^{2-}_{4(aq)} + 4H^+_{(aq)} \qquad (3)$$

$$4Fe^{2+}_{(aq)} + O_{2(aq)} + 4H^+_{(aq)} \rightarrow 4Fe^{3+}_{(aq)} + 2H_2O \qquad (4)$$

$$FeS_2 + 14Fe^{3+}_{(aq)} + 8H_2O \rightarrow 15Fe^{2+}_{(aq)} + 2SO^{2-}_{4(aq)} + 16H^+_{(aq)} \qquad (5)$$

The first step, Equation 3, results in release of sulfate and Fe^{2+} ions into solution. This is because sulfur oxidation occurs more readily than iron oxidation. The Fe^{2+} ions released become available for the iron oxidation step in Equation 4. Equation 5 is a secondary pyrite oxidation mechanism where Fe^{3+} ions, typically sourced from the Equation 4 step, act as the oxidizing agent. With continued oxidation, the Fe^{2+} ions released in Equation 5 will recycle through the Equation 4 step.

Such reactions result in characteristic assemblages of secondary precipitates, based on Fe III sulfates, sulfate hydrates, and oxyhydroxides (Bigham and Nordstrom 2000). The fracture assemblage associated with the pyrite remnants and pseudomorphs is consistent with this (goethite, lepidocrocite–oxyhydroxides, jarosite, natrojarosite–sulfate hydrates). The low-pH conditions generated by pyrite oxidation are expected to result in the dissolution of acid-sensitive minerals. The observed carbonate removal and depletion immediately adjacent to the iron-based fracture mineralization in this study fit this expectation, and the potassium and sodium required for the jarosites may come from the dissolution of silicates (clays, feldspars). The textural, mineralogical, and spatial relationships of the fracture mineralizations are therefore consistent with our hypothesis.

The detection of arsenic both in the pyrite remnants and in patches of associated iron oxide–hydroxide mineralization also supports the hypothesis and link the phases paragenetically. Fully oxidized arsenic (As V) is expected to co-precipitate with or be sorbed by the secondary alteration products of the pyrite oxidation process, such as goethite and jarosite (Savage et al. 2000). It has been suggested that the presence of significant arsenic in the pyrite structure may increase the rate of oxidation of the pyrite (Savage et al. 2000; Blanchard et al. 2007).

Stress Environment

The fabrics associated with the jarosite-bearing fracture mineralization, such as the local absence of detrital grains, the fracture-perpendicular shape and orientation of jarosite domains, and the fracture-perpendicular trails of grain fragments, are all textures developed during the opening of the fractures. This inference is also supported by the local presence of fracture-parallel grain fracturing cemented by the secondary, pyrite-oxidation-related, Fe III phases, suggesting further that the oxidative episode occurred contemporaneously with the reactivation of pyrite-mineralized fractures under a tensional environment. Similar textures developed in the late-stage gypsum-cemented fractures are subparallel to the jarosite- and Fe III-defined textures, suggesting a similar, fracture-opening regime applied during their formation.

Fracture Paragenesis

A clear paragenesis can be determined from the field observations and the detailed petrography. Pyrite remnants and pseudomorphs are central to the fracture assemblages and are clearly the first identifiable fracture-related mineralization. They occur in relatively tightly constrained planes, but there are multiple parallel and subparallel occurrences at each sample site. The pyrite host fractures were normal faults.

Following the evidence presented above, oxidation of the pyrite and reactivation of the pyrite-mineralized fractures are contemporaneous episodes and occurred in Mode 1 fractures that would have allowed preferential movement of fluids along them. It is not possible to deduce if the fluids were downward- or upward-flowing. Precipitation of the Fe-based mineralization occurred during this period, including the formation of jarosite, goethite, lepidocrocite, and hematite. At some sites Al oxide and/or hydroxide also formed.

Field relationships show that the gypsum- and calcite-cemented fractures postdate the Fe-mineralized fractures; indeed they appear to be the last fracture-mineralization events at the studied sites. These relationships are confirmed by the detailed petrography; fragments of the iron-mineralization assemblage are entrained within the gypsum cement, and calcite-cemented fractures cut through the iron mineralization. The calcite of the fractures is distinctly different from the host rock carbonates, having none of the complex internal CL- and CCI-resolvable micro-textures. This, and the fact that the calcite fractures cut across the carbonate removal and depletion zones, distinguishes the fracture calcite paragenetically.

Locally, the calcite-cemented fractures terminate against gypsum-cemented fractures, and there are fragments of the calcite cement enclosed by gypsum, suggesting that at least some of the gypsum-cemented fractures postdate the calcite-cemented fractures. Field relationships suggest that there is, however, some overlap of these two phases.

The cross-fiber texture common to the gypsum veins is typical of those described to have formed by the crack-seal mechanism (Ramsay 1980), the implication being that the fracture dilation is coeval with mineralization.

Field relationships also show that these fractures feed carbonate-sulfate travertine deposits in the study area which have been dated to have formed within the last 400,000 years (Kampman et al. 2012). Kampman et al. (2012) identified pulses of CO_2 emissions from intracrustal faults following climatic warming episodes at glacial-to-interglacial transitions, suggesting that crustal flexure resulting from the unloading of ice during these episodes provided enhanced pathways for buoyant fluids. Our observations of multiple, Mode 1, reactivations of the fractures are consistent with their hypothesis.

Pyrite Pseudomorphs

Observed variations in the textures of jarosite and iron oxide–hydroxide mineralization most likely result from variations in the distribution of pre-oxidation-event minerals (pyrite, carbonates) and porosity as well as subsequent diagenetic alteration of the mineralization phases themselves. For example, it has been suggested that pseudomorphing of pyrite by Fe oxyhydroxides (Fig. 8), occurs only when there is sufficient localized alkalinity to neutralize the acid generated by pyrite oxidation (Huminicki and Rimstidt 2009), particularly during the early part of the process. The rate of oxidation of Fe^{2+} is inhibited at low pH (Bigham and Nordstrom 2000). Consequently, where the pH is not neutralized, a high proportion of the Fe^{2+} created by the first stage of the oxidation of the pyrite would be released into solution, before further oxidation more distally from the "host" pyrite, and pseudomorph development would not occur. Where neutralization does occur, Fe^{2+} oxidation is not inhibited and the almost immediate precipitation of FeOOH is forced; this in turn forms a layer that increasingly moderates the oxidation as the reaction progresses. These conditions are generally satisfied only if there is a sufficient supply of neutralizing agent to balance the acid being generated to maintain a nearly neutral pH. The carbonate cement that would have been present in the host rock before pyrite oxidation is a potential source of a neutralizing agent; its patchy distribution may therefore explain the patchy presence of well-developed pyrite pseudomorphs.

Jarosite

Jarosite forms under conditions of low pH and high Eh, and is commonly associated with the surface oxidation (weathering) of pyrite in the presence of aluminosilicates (Long et al. 1992; Bingham and Nordstrom 2000). Its presence is an indicator of the earlier presence of sulfide minerals (Bladh 1982; Long et al. 1992; Bigham and Nordstrom 2000; Bell and Bowen 2014). As fragments of the jarosite-bearing iron mineralization assemblage are enclosed within gypsum-cemented fractures (Fig. 7E), then we can categorically state that the jarosite observed here is not a by-product of recent weathering, but must have formed before the late sulfate- and carbonate-cemented fractures.

Much of the jarosite occurs in domains where it is closely intergrown with stringers and rims of iron oxide–hydroxide, probably a result of their co-precipitation during pyrite alteration. Jarosite is a relatively soluble mineral, and there is clear evidence of some dissolution. Some of the iron oxide–hydroxide deposits outline pores or porous jarosite domains. Jarosite dissolution results in the localized formation of goethite (Elwood Madden et al. 2012). Some of the iron oxide–hydroxide–jarosite intergrowths (Fig. 7C) are therefore most likely "secondary" after partial dissolution. The low-permeability rims may have protected the remaining jarosite from further dissolution (Smith et al. 2006); this and the modern arid climate at the outcrop sites has resulted in the preservation of the jarosite.

Bell and Bowen (2014) report on a significant outcrop of jarosite-cemented Navajo Sandstone that is associated with regional-scale bleaching. They attribute the presence of jarosite to the oxidative alteration of an unidentified sulfide during uplift, shortly before exhumation. The similarity of the mineral assemblages (including the presence of arsenic) and the association with bleaching at their site suggest that the observations made at our sites may have a larger regional relevance. Application of similar petrographic techniques may reveal further parallels. From our observations, jarosite appears to be more robust than they suggest, perhaps through shielding by associated iron oxide–hydroxides, allowing a model of earlier, deeper sulfide oxidation and jarosite precipitation.

Carbonates

An expected effect of the oxidative alteration of pyrite is the localized dissolution of carbonate minerals through the formation of sulfuric acid (see section on pyrite oxidation and Equation 2 above). The observed zones of carbonate removal and depletion in the fracture wall rock are both consistent with, and add further weight to, our hypothesis. The zones of carbonate removal and depletion run parallel to the Fe-mineralized parts of the fracture systems (e.g., Fig. 6C, D) and are of varied thicknesses both at and between sample sites. In the zones of depletion, dolomite is the carbonate phase that is detected closest to the fracture, reflecting its lower solubility than calcite at low pH values. An expected by-product of reactions between calcium-bearing carbonates and sulfuric acid is calcium sulfate, and the presence of common gypsum as a cement in these zones is consistent with this, although it is recognized that alternative sources of this gypsum (e.g., recent fracture mineralization) mean that it is not necessarily present as a result of this reaction.

The only carbonate detected in the carbonate-removal zones is calcite associated with paragenetically late fractures that crosscut the iron-based mineralization. This relationship firmly places this fracture calcite formation as a post-oxidative pyrite alteration event. The presence of Mn in this late calcite cement constrains the Eh conditions of formation to those where Mn^{2+} can exist, i.e., at least periodically reducing.
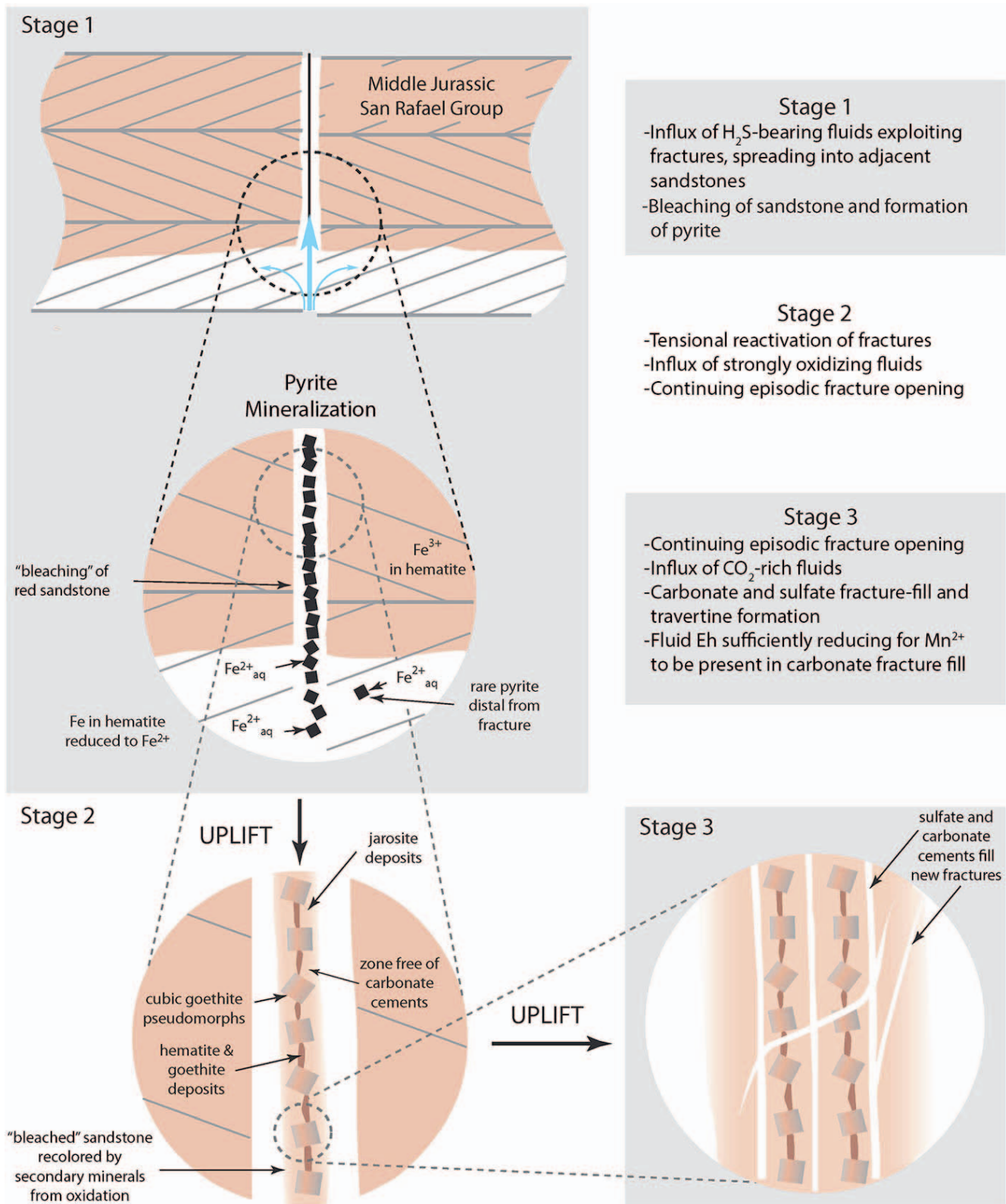
FIG. 9.—Summary paragenetic sequence for the formation and mineralization of the fractures of the study area.

No siderite was detected at any of the sites, and Fe was not detected in the late fracture calcite. This suggests that during the most recent period of carbonate precipitation, conditions were not reducing enough for Fe II to be produced from the abundant Fe III species present in the fracture system.

PARAGENETIC SEQUENCE OF FRACTURE MINERALIZATION

The paragenetic sequence of the fracture mineralization (Fig. 9) indicates that the bleaching of the fractures and fracture-adjacent host rocks occurred during a diagenetic episode related to pyrite formation. The paragenetic relationships show that this event was the first mineralization episode associated with the fractures.

Red-bed bleaching of the type shown in the study area is a two-part process, first requiring the reduction of the Fe III in hematite present in grain coatings, then requiring mobilization of the resultant Fe II. The concentration of the pyrite along the fracture is the most likely destination of the Fe II mobilized in this manner, probably along a diffusion gradient set up at the onset of pyrite precipitation, as described above.

We consider it likely that the larger-scale, regional bleaching of the Entrada Sandstone was as a consequence of a similar H_2S-driven mechanism to the fractures, but we recognize that there is insufficient evidence from this study to make this extrapolation anything other than speculation.

CONCLUSIONS

In this study we have shown that in the Middle Jurassic red-bed Entrada Sandstone of the Salt Wash Graben area of Utah, USA, fractures have been reactivated many times and exploited by several distinct fluids, each of which has left a unique diagenetic fingerprint. The following three main diagenetic episodes have been identified:

1. *Red-bed bleaching and pyrite formation*. Bleaching resulted from the removal of hematite by strongly reducing fluids preferentially channeled along fractures. Pyrite formed from the resulting Fe II and was arsenic-bearing. H_2S is suggested as a likely combined reducing agent and S source, potentially associated with hydrocarbon generation and/or movement as indicated by localized bituminous deposits.
2. *Reactivation of fracture system under tensional environment, oxidation of pyrite*. Key indicators of pyrite oxidation are the presence of jarosite, pyrite pseudomorphs, iron oxide–hydroxide, and carbonate-dissolution zones. A tensional environment is shown by grain fracturing and spreading as well as by elongation of mineral forms perpendicular to the fracture orientation.
3. *Multiple tensional re-activations of fractures, cemented by carbonate and sulfate*. The carbonate and sulfate cements are linked to cliff-top travertine deposits and contain fragments of the oxidized pyrite mineral assemblages. A tensional environment is indicated by the cross-fiber gypsum cement. Traces of Mn in the carbonate without Fe point to slightly reducing fluids. We propose that this episode is linked to the CO_2-rich fluids.

It is possible that the original bleaching and pyrite formation event occurred a considerable time before the subsequent fracture reactivations.

Since the later pyrite oxidation event and subsequent carbonate- and sulfate-hosted fracture reactivations all occurred under similar tensional tectonic environments, they may be associated with the mechanism identified by Kampman et al. (2012), related to repeated interglacial warming unloading intraplate flexures during the last 400,000 years.

Similarities in the mineral assemblages (including the presence of arsenic) and the association with bleaching at a significant outcrop of jarosite-cemented Entrada Sandstone in the Grand Staircase–Escalante National Monument (Bell and Bowen 2014) suggest that the observations made in our study may have a larger regional relevance. Our identification of a pyrite mineralization event provides a possible identification of the "unidentified sulphide" at their site.

This study highlights the complexity of interpreting analogue sites. An association of fluid chemistry (e.g., CO_2-rich brines) with textural and mineralogical features (e.g., bleaching) may be juxtaposed spatially but not temporally. Preferential fluid pathways, be they due to inherent sediment characteristics (grain size, sorting, clay content, presence of syndepositional cements) or to diagenetic overprint (cementation, dissolution, fracturing), will be exploited by many different fluids over geological time periods.

SUPPLEMENTAL MATERIAL

Supplemental Materials are available from the SEPM Data Archive: https://www.sepm.org/supplemental-materials.

REFERENCES

ALLIS, R., CHIDSEY, T., GWYNN, W., MORGAN, C., WHITE, S., ADAMS, M., AND MOORE, J., 2001, Natural CO_2 reservoirs on the Colorado Plateau and Southern Rocky Mountains: candidates for co_2 sequestration: Washington, D.C., First National Conference on Carbon Sequestration, Proceedings, 19 p.

ALLIS, R.G., MOORE, J.H., CHIDSEY, T., MORGAN, C., GWYNN, W., DOELLING, H.H., ADAMS, M., RAUZI, S., AND WHITE, S.P., 2002, CO_2 geysers, springs, and massive travertine deposits on the Colorado Plateau: examples of natural leakage of fluids saturated in CO_2, [Abstract]: Geological Society of America, Abstracts with Programs, v. 34, p. 392.

BAINES, S.J., AND WORDEN, R.H., 2004, The long-term fate of CO_2 in the subsurface: natural analogues for CO_2 storage, in Baines, S.J., and Worden, R.H., eds., Geological Storage of Carbon Dioxide: Geological Society of London, Special Publication 233, p. 59–85.

BELL, J.H., AND BOWEN, B.B., 2014, Fracture-focused fluid flow in an acid and redox-influenced system: diagenetic controls on cement mineralogy and geomorphology in the Navajo Sandstone: Geofluids, v. 14, p. 251–265.

BIGHAM, J.M., AND NORDSTROM, D.K., 2000, Iron and aluminum hydroxysulfates from acid sulfate waters, in Ribbe, P.H., ed., Reviews in Mineralogy and Geochemistry: Sulfate Minerals, p. 351–403.

BLADH, K.W., 1982, The formation of goethite, jarosite, and alunite during the weathering of sulfide-bearing felsic rocks: Economic Geology, v. 77, p. 176–184.

BLANCHARD, M., ALFREDSSON, M., BRODHOLT, J., WRIGHT, K., AND CATLOW, C.R.A., 2007, Arsenic incorporation into FeS_2 pyrite and its influence on dissolution: a DFT study: Geochimica et Cosmochimica Acta, v. 71, p. 624–630.

BREIT, G.N., AND GOLDHABER, M.B., 1996, Diagenesis of sandstones in the Morrison Formation within the Paradox Basin, in Huffman, A.C.J., Lund, W.R., and Godwin, L.H., eds., Geology and Resources of the Paradox Basin: Utah Geological Association, Guidebook 25, p. 197–210.

CHAN, M.A., PARRY, W.T., AND BOWMAN, J.R., 2000, Diagenetic hematite and manganese oxides and fault-related fluid flow in Jurassic Sandstones, southeastern Utah: American Association of Petroleum Geologists, Bulletin, v. 84, p. 1281–1310.

CHAN, M.A., PARRY, W.T., PETERSEN, E.U., AND HALL, C.M., 2001, Ar-40/Ar-39 age and chemistry of manganese mineralization in the Moab and Lisbon fault systems, southeastern Utah: Geology, v. 29, p. 331–334.

CRABAUGH, M., AND KOCUREK, G., 1993, Entrada Sandstone: an example of a wet aeolian system, in Pye, K., ed., The dynamics and environmental context of aeolian sedimentary systems: Geological Society of London, Special Publication 72, p. 103–126.

DOELLING, H.H., 2001, Geologic map of the Moab and eastern part of the San Rafael Desert, Grand and Emery counties, Utah and Mesa County, Colorado, 30′ × 60′ Quadrangle: Utah Geological Survey, Geologic Map 180, 1:100,000 scale.

DOELLING, H.H., 2002, Geologic Map of the San Rafael Desert, Emery and Grand counties, Interim, Utah, 30′ × 60′ Quadrangle: Utah Department of Natural Resources, 1:100,000 scale.

EICHHUBL, P., DAVATZES, N.C., AND BECKER, S.P., 2009, Structural and diagenetic control of fluid migration and cementation along the Moab fault, Utah: American Association of Petroleum Geologists, Bulletin, v. 93, p. 653–681.

ELWOOD MADDEN, M.E., MADDEN, A.S., RIMSTIDT, J.D., ZAHRAI, S., KENDALL, M.R., AND MILLER, M.A., 2012, Jarosite dissolution rates and nanoscale mineralogy: Geochimica et Cosmochimica Acta, v. 91, p. 306–321.

FOXFORD, K.A., GARDEN, I.R., GUSCOTT, S.C., BURLEY, S.D. LEWIS, J.M., WALSH, J.J., AND WATTERSON, J., 1996, The field geology of the Moab Fault, in Huffman, A.C.J., Lund, W.R., and Godwin, L.H., eds., Geology and Resources of the Paradox Basin, Utah Geological Association, Guidebook 25, p. 265–283.

GARDEN, I.R., GUSCOTT, S.C., BURLEY, S.D., FOXFORD, K.A., WALSH, J.J., AND MARSHALL, J., 2001, An exhumed palaeo-hydrocarbon migration fairway in a faulted carrier system, Entrada Sandstone of SE Utah, USA: Geofluids, v. 1, p. 195–213.

GARRELS, R.M., AND THOMPSON, M.E., 1960, Oxidation of pyrite by iron sulfate solution: American Journal of Science, v. 258A, p. 57–67.

GRIFFIN, B.J., 2000, Charge contrast imaging of material growth and defects in environmental scanning electron miscroscopy: linking electron emission and cathodoluminescence: Scanning, v. 22, p. 234–242.

HASZELDINE, R.S., QUINN, O., ENGLAND, G., WILKINSON, M., SHIPTON, Z.K., EVANS, J.P., HEATH, J., CROSSEY, L., BALLENTINE, C.J., AND GRAHAM, C.M., 2005, Natural geochemical analogues for carbon dioxide storage in deep geological porous reservoirs, a United Kingdom perspective: Oil & Gas Science and Technology, v. 60, p. 33–49.

HILLIER, S., 1999, Use of an air-brush to spray dry samples for X-ray powder diffraction: Clay Minerals, v. 34, p. 127–135.

HILLIER, S., SUZUKI, K., AND COTTER-HOWELLS, J., 2001, Quantitative determination of cerussite (lead carbonate) by X-ray powder diffraction and inferences for lead speciation and transport in stream sediments from a former lead mining area in Scotland: Applied Geochemistry, v. 16, p. 597–608.

HINTZE, L.F., 1988, Geologic history of Utah: Brigham Young University, Geology Studies, Special Publication 7.

HUMINICKI, D.M.C., AND RIMSTIDT, J.D., 2009, Iron oxyhydroxide coating of pyrite for acid mine drainage control: Applied Geochemistry, v. 24, p. 1626–1634.

IPCC, 2005, Carbon Dioxide Capture and Storage: Special Report of the Intergovernmental Panel on Climate Change, Cambridge University Press.

IPCC, 2014, Climate Change 2014: Synthesis Report: Contribution of Working Groups I, II, and III to the Fifth Assessment Report of the Intergovernmental Panel on Climate Change: Geneva, 155 p.

KAMPMAN, N., BICKLE, M., BECKER, J., ASSAYAG, N., AND CHAPMAN, H., 2009, Feldspar dissolution kinetics and Gibbs free energy dependence in a CO_2-enriched groundwater system, Green River, Utah: Earth and Planetary Science Letters, v. 284, p. 473–488.

KAMPMAN, N., BURNSIDE, N.M., SHIPTON, Z.K., CHAPMAN, H.J., NICHOLL, J.A., ELLAM, R.M., AND BICKLE, M.J., 2012, Pulses of carbon dioxide emissions from intracrustal faults following climatic warming: Nature Geoscience, v. 5, p. 352–358.

KAMPMAN, N., BICKLE, M., WIGLEY, M., AND DUBACQ, B., 2014, Fluid flow and CO_2–fluid–mineral interactions during CO_2-storage in sedimentary basins: Chemical Geology, v. 369, p. 22–50.

KOCUREK, G., 1981, ERG reconstruction: The Entrada sandstone (Jurassic) of northern Utah and Colorado: Palaeogeography, Palaeoclimatology, Palaeoecology, v. 36, p. 125–153.

LONG, D.T., FEGAN, N.E., MCKEE, J.D., LYONS, W.B., HINES, M.E., AND MACUMBER, P.G., 1992, Formation of alunite, jarosite and hydrous iron-oxides in a hypersaline system: Lake Tyrrell, Victoria, Australia: Chemical Geology, v. 96, p. 183–202.

MCKNIGHT, E.T., 1940, Geology of area between Green and Colorado rivers, Grand and San Juan counties, Utah: U.S. Geological Survey, Bulletin 908, 147 p.

MILODOWSKI, A.E., AND RUSHTON, J.C., 2008, Mineralogical and porosity characterisation of potential aquifer and seal units for carbon capture and storage methodologies for the CASSEM Project: British Geological Survey, Commissioned Report CR/08/153N, 75 p.

NEWELL, A.J., AND BUTCHER, A.S., 2015, Sedimentological control on the reservoir and caprock properties of a bleached palaeoreservoir in the Entrada Formation at Salt Wash Graben, Green River, Utah: British Geological Survey, Open Report OR/15/005, 45 p.

NUCCIO, V.F., AND CONDON, S.M., 1996, Burial and thermal history of the Paradox Basin, Utah and Colorado, and petroleum potential of the Middle Pennsylvanian Paradox Formation: U.S. Geological Survey, Bulletin 2000, 44 p.

OGATA, K., SENGER, K., BRAATHEN, A., AND TVERANGER, J., 2014, Fracture corridors as seal-bypass systems in siliciclastic reservoir-cap rock successions: field-based insights from the Jurassic Entrada Formation (SE Utah, USA): Journal of Structural Geology, v. 66, p. 162–187.

PARRY, W.T., FORSTER, C.B., EVANS, J.P., BOWEN, B.B., AND CHAN, M.A., 2007, Geochemistry of CO_2 sequestration in the Jurassic Navajo Sandstone, Colorado Plateau, Utah: Environmental Geosciences, v. 14, p. 91–109.

PARRY, W.T., CHAN, M.A., AND NASH, B.P., 2009, Diagenetic characteristics of the Jurassic Navajo Sandstone in the Covenant oil field, central Utah thrust belt: American Association of Petroleum Geologists, Bulletin, v. 93, p. 1039–1061.

PACALA, S., AND SOCOLOW, R., 2004, Stabilization wedges: solving the climate problem for the next 50 years with current technologies: Science, v. 305, p. 968–972.

PEARCE, J.M., HOLLOWAY, S., WACKER, H., NELIS, M.K., ROCHELLE, C., AND BATEMAN, K., 1996, Natural occurrences as analogues for the geological disposal of carbon dioxide: Energy Conversion and Management, v. 37, p. 1123–1128.

RAMSAY, J.G., 1980, The crack seal mechanism of rock deformation: Nature, v. 284, p. 135–139.

ROCHELLE, C., BATEMAN, K., AND PEARCE, J.M., 2002, Geochemical interactions between supercritical CO_2 and the Utsira formation: an experimental study: British Geological Survey, Commissioned Report CR/02/060, 57 p.

SAVAGE, K.S., TINGLE, T.N., O'DAY, P.A., WAYCHUNAS, G.A., AND BIRD, D.K., 2000, Arsenic speciation in pyrite and secondary weathering phases, Mother Lode Gold District, Tuolumne County, California: Applied Geochemistry, v. 15, p. 1219–1244.

SCHMIDT, V., AND MCDONALD, D.A., 1979, The role of secondary porosity in the course of sandstone diagenesis: SEPM, Special Publication 26, p. 175–207.

SHIPTON, Z.K., EVANS, J.P., KIRSCHNER, D., KOLESAR, P.T., WILLIAMS, A.P., AND HEATH, J., 2004, Analysis of CO_2 leakage through "low-permeability" faults from natural reservoirs in the Colorado Plateau, southern Utah, in Baines, S.J., and Worden, R.H., eds., Geological Storage of Carbon Dioxide: Geological Society of London, Special Publication 233, p. 43–58.

SINGER, P.C., AND STUMM, W., 1970, Acidic Mine Drainage: The Rate-Determining Step: Science, v. 167, p. 1121–1123.

SMITH, A.M.L., HUDSON-EDWARDS, K.A., DUBBIN, W.E., AND WRIGHT, K., 2006, Dissolution of jarosite [KFe3(SO4)2(OH)6] at pH 2 and 8: insights from batch experiments and computational modelling: Geochemica et Cosmochimica Acta, v. 70, p. 608–621.

SNYDER, R.L., AND BISH, D.L., 1989, Quantitative analysis, in Bish, J.L., and Post, J.E., eds., Modern Powder Diffraction: Mineralogical Society of America, Reviews in Mineralogy, v. 20, p. 101–144.

STOFFREGEN, R.E., ALPERS, C.N., AND JAMBOR, J.L., 2000, Alunite–jarosite crystallography, thermodynamics, and geochronology, in Alpers, C.N., Jambor, J.L., and Nordstrom, D.K., eds., Sulfate Minerals: Crystallography, Geochemistry, and Environmental Significance: Reviews in Mineralogy and Geochemistry, v. 40, p. 453–479.

STOKES, W.L., 1986, Geology of Utah: Utah Museum of Natural History, University of Utah and Utah Geological and Mineral Survey, Department of Natural Resources, Salt Lake City, Utah, 307 p.

WALKER, T.R., 1967, Formation of red beds in modern and ancient deserts: Geological Society of America, Bulletin, v. 78, p. 353–368.

WALKER, T.R., WAUGH, B., AND GRONE, A.J., 1978, Diagenesis in 1st-cycle desert alluvium of Cenozoic age, southwestern United States and northwestern Mexico: Geological Society of America, Bulletin, v. 89, p. 19–32.

WEIBEL, R., KJOLLER, C., BATEMAN, K., LAIER, T., NIELSEN, L.H., AND PURSER, G., 2014, Carbonate dissolution in Mesozoic sand- and claystones as a response to CO_2 exposure at 70 degrees C and 20 MPa: Applied Geochemistry, v. 42, p. 1–15.

WIGLEY, M., KAMPMAN, N., DUBACQ, B., AND BICKLE, M., 2012, Fluid–mineral reactions and trace metal mobilization in an exhumed natural CO_2 reservoir, Green River, Utah: Geology, v. 40, p. 555–558.

WIGLEY, M., DUBACQ, B., KAMPMAN, N., AND BICKLE, M., 2013, Controls of sluggish, CO_2-promoted, hematite and K-feldspar dissolution kinetics in sandstones: Earth and Planetary Science Letters, v. 362, p. 76–87.

WILSON, M.D., 1992, Inherited grain-rimming clays in sandstones from eolian and shelf environments: their origin and control on reservoir properties, in Houseknecht, D.W., and Pittman, E.D., eds., Origin, Diagenesis, and Petrophysics of Clay Minerals in Sandstones: SEPM, Special Publication 47, p. 209–225.

ZHOU, Z., BALLENTINE, C.J., SCHOELL, M., AND STEVENS, S.H., 2012, Identifying and quantifying natural CO_2 sequestration processes over geological timescales: the Jackson Dome CO_2 deposit, USA: Geochimica et Cosmochimica Acta, v. 86, p. 257–275.

ZOLOTOV, M.Y., AND SHOCK, E.L., 2005, Formation of jarosite-bearing deposits through aqueous oxidation of pyrite at Meridiani Planum, Mars: Geophysical Research Letters, v. 32., no. 21, L21203.